ORIGINAL ARTICLE

Study on "pull-shear" material removal principle and novel compound structure tool design during cutting KFRP

Fei Su[1,2] · Guangtao Liu[1,2] · Ke Zhang[3] · Xun Ding[3] · Changliang Gong[4]

Abstract
The Kevlar fiber-reinforced polymer (KFRP) is widely used in various fields due to its excellent mechanical and physical properties. However, the material is prone to processing defects such as burring and furry during secondary processing. In this paper, based on the cutting removal mechanism of KFRP, a "pull-shear" material removal principle for the residual fibers was proposed and analyzed. Then, a novel compound structure milling tool was designed. Theoretical and experimental analyses of the milling tests were carried out on the plain-woven KFRP composites. The result indicates that when the fibers are subjected to tension, the cutting surface quality is significantly improved. Therefore, when the "pull-shear" removal principle can be implemented effectively, the fibers can be effectively cut off in time. The "pulling-shearing" effect can be effectively implemented by the novel compound structure milling tool. The milling surface quality of the novel compound structure milling tool is better than the conventional tools. The burr defect factor gradually decreases with the increase of the feed speed. The burr defect factors tend to increase with the increase in cutting speed.

1 Introduction

At present, Kevlar fiber-reinforced polymer (KFRP) is widely used in aerospace, military, and other fields because of its unique properties, such as its high strength-to-mass ratio and modulus. Although the fabrication of KFRP members is generally close to the final shape of the component, a variety of subsequent machining operations are usually required to achieve the final specifications for assembly

✉ Fei Su
sfeihe@163.com

1   Hunan Provincial Key Laboratory of High Efficiency and Precision Machining of Difficult-to-Cut Material, Hunan University of Science and Technology, Xiangtan 411201, China

2   Intelligent Manufacturing Institute of HNUST, Hunan University of Science and Technology, Xiangtan 411201, China

3   Jiangnan Industrial Group Co., Ltd, Xiangtan 411207, China

4   Hunan SUND Technological Corporation, Xiangtan 411201, China

[1–3]. However, as a typically difficult material to process, KFRP is prone to defects such as drawing, delamination, tearing, and thermal damage in actual processing [4, 5]. Therefore, many scholars have carried out a lot of research on the processing of KFRP.

Among them, the material properties of fiber and resin matrix are different, resulting in the processing mechanism of KFRP is more complicated. Therefore, the processing mechanism of FRP is one of the research hotspots of scholars. Shi et al. [6] pointed out that fiber orientation is one of the important factors affecting the cutting mechanism of Kevlar fiber. Liu et al. [7] found that the fracture of Kevlar fiber is significantly different from that of carbon fiber through the milling test of AFRP. The fracture of Kevlar fiber requires greater shear force and presents an obvious ductile fracture. Talib et al. [8] analyzed the influence of fiber distribution angles on the tensile load properties of Kevlar composites. They determined the final failure load of each fiber distribution with the method of finite element simulation and tensile tests. Shuaib et al. [9] verified the effect of different processing parameters on the change of cutting force and torque by drilling test. They presented that the outlet of the drilling hole was rougher than the entrance, and the processing quality and residual fiber length of the

outlet hole decreased with the increase in thickness. When the rotational speed and feed velocity are small, it is easier to have fibers remaining on the surface. Teti [10] summarized the processing characteristics of composite materials and introduced some special processing methods. Yilbas et al. [11] conducted experimental research on hole machining of aramid fiber composites with different diameters and analyzed the factors affecting the machining quality in the cutting process. Shi et al. [12] conducted a series of AFRP milling experiments to study two different delamination defects, viz., tear delamination and uncut delamination. Aimed at two different types of stratification, a calculation method and model based on brittle fracture are established. The results can be used to explain the mechanism and rule of the formation of stratified defects. The control strategy of layered defects and the evaluation method of finished product surface integrity are further discussed. Wang et al. [13] studied the optimization of machining parameters for milling KFRP. Wang et al. [14] established a theoretical model for predicting milling force. They indicated that the milling parameters such as tool front angle, fiber direction angle, and cutting depth have significant effects on the change of milling force.

As an essential means to study, the finite element simulation is widely used in the study of the processing mechanism of fiber-reinforced composites. Dandekar and Shin [15] established a two-dimensional microscopic simulation model consisting of fiber, resin, and zero-thickness interfaces. The research results showed that the cracking degree of resin and the damage degree of fiber increased with the increase of fiber angle. Calzada et al. [16] adopted a continuous solid element to simulate the interface phase so as to avoid the distortion of zero-thickness interface elements. With the help of the model, the fiber failure mode, chip length, and cutting force under different fiber angles were investigated. Xu et al. [17] proposed a two-dimensional cutting model of KFRP to analyze the cutting stress field and damage depth. Cheng et al. [18] presented a micro-scale, thermo-mechanically coupled cutting model for UD CFRP. Chen et al. [19] found the 3D finite element models, including macro and micro models for CFRP cutting. Based on four typical fiber orientation angles (FOAs), the micro-failure mechanism of CFRP and the formation mechanism of macro-chips under cutting load are studied. Xu et al. [20] established a unidirectional CFRP finite element right-angle cutting model with a variable friction coefficient to analyze the cutting mechanism of CFRP materials. Alessandro et al. [21] published a cohesive model. In their model, a new approach for representing the fiber-matrix interface is proposed for a three-dimensional FE model of orthogonal cutting of UD-CFRP. Meng et al. [22] built a three-dimension micro-scale cutting simulation model. The experiment and simulation were combined to analyze the evolution and the correlation of cutting forces, machined surface roughness, sub-surface damage, and burr formation.

In addition, in order to solve the various defects in the processing of fiber-reinforced composite materials, the design of special cutting tools for fiber-reinforced composite materials has attracted the attention of many scholars. Bhattacharyya and Horrigan [23] used an improved high-speed steel twist drill to drill KFRP. Under the condition of liquid nitrogen cooling, the machining quality of the improved tool is better than that of the unimproved tool. Yan et al. [24] believed that choosing a large-diameter milling tool with a large rake angle or relief angle for high-speed cutting can effectively improve the quality of the AFRP milling entrance and section. Qi [25] established an optimization model of KFRP based on cutting test data using the linear regression method. Liu et al. [7] studied the effects of different spiral angles and cutting tool structures on cutting force and machining surface quality through AFRP milling experiments. They claimed that the cutting tool geometry can have a greater influence on machined surface quality than the cutting parameters. Swan et al. [26] reported the effects of the tool coating on the processing. Jia et al. [27] proposed a novel drill structure to change the cutting conditions at the drill exit and effectively reduce damages during the drilling of CFRP. In their tool structure design, the cutting lips of the structure reverse the cutting direction from downward to upward; then, the drill-exit damages can be completely suppressed. Qiu et al. [28] studied the drilling characteristics of the dagger drill, the double point angle drill, and the candle stick drill. Then, a new tool is developed for drilling CFRP based on the advantages of the three kinds of drill bits. The result shows that the new compound drill bit can effectively remove fibers and reduce thrust force at the drilling exit stage, form burr-free and small delamination hole.

In summary, the current research on the processing mechanism of fiber-reinforced composite materials and the cutting effects of the related special tools has been studied in depth. Among them, a lot of studies about the tool material and tool structures are conducted. However, the current tool structure design is mostly based on the experience, and the research on the combination of the tool structure design and the principle of material removal is rarely reported. In this paper, according to the cutting removal mechanism analysis of KFRP fiber, a cutting principle of "pull-shear" material removal was proposed. Then, the effectiveness of this principle of material removal was verified by the airflow field simulation and cutting simulation during the cutting KFRP. According to this cutting principle of "pull-shear" material removal, a novel compound structure milling tool was designed and manufactured by combining the fish-scale micro-tooth structure with the PCD material cutting edge. Simultaneously, a series of KFRP machining experiments

were carried out. The changing rules of machining quality, cutting force, and temperature were analyzed.

2 "Pull-shear" removal principle and tool design concept

2.1 "Pull-shear" removal principle

When the tool is in contact with the fiber, the cutting force F_c can be divided into axial F_t and tangential F. In the contact zone, the fiber is mainly subjected to contact stress, bending stress, tensile stress, and shear stress, which is shown in Fig. 1. When the bending stress reaches its maximum, the fibers are bent, but no bending fracture occurs at this time.

With the tool feed, the tensile and contact stresses of the fiber are increasing; the shear and bending stresses are decreasing. This makes it difficult for shear fracture to occur until the fiber exceeds the strength limit and tensile fracture occurs, as in Fig. 1a. If a tensile F_T is added along the axial direction of the fiber, then the fiber in the contact area is also subjected to contact stress, bending stress, tensile stress, and shear stress. The tensile stress and bending stress are larger than the other stresses, as in Fig. 1b. With the tool feed, the

materials in the contact area are gradually compressed. At the same time, the axial area of the fiber is reduced by tensile deformation. Tensile and shear stresses will increase, so the fiber is prone to shear fracture in the contact area. It can be seen that applying a certain tensile stress in the axial direction of the fiber can restrain the fiber bending and make the fiber more prone to shear fracture. The stress required to break the material is reduced, and the cutting force F_c and tangential force F are smaller.

### 2.2 Design of novel compound tool structure

In order to realize the "pull-shear" removal principle described above, an axial tension F_T is applied to the fiber during the cutting. To provide axial tension on the fiber in the cutting process, a novel special tool with "pull-shear" removal principle combined with the existing tool structure is designed.

The cutting edge of the existing fish-scale milling tool is composed by some small cutting edges with different turns. According to the test observation, the numerous fish-scale micro-teeth of the fish-scale milling cutter are involved in mill processing during the milling. The cutting depth of each cutting edge is small, then the cutting forces can be

Fig. 1 Schematic diagram of pull-shear removal principle
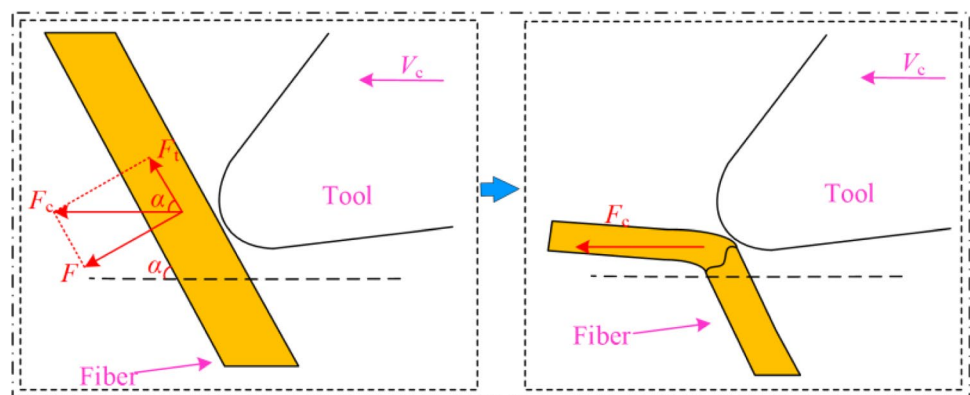
(a) Fiber breakage without tension force
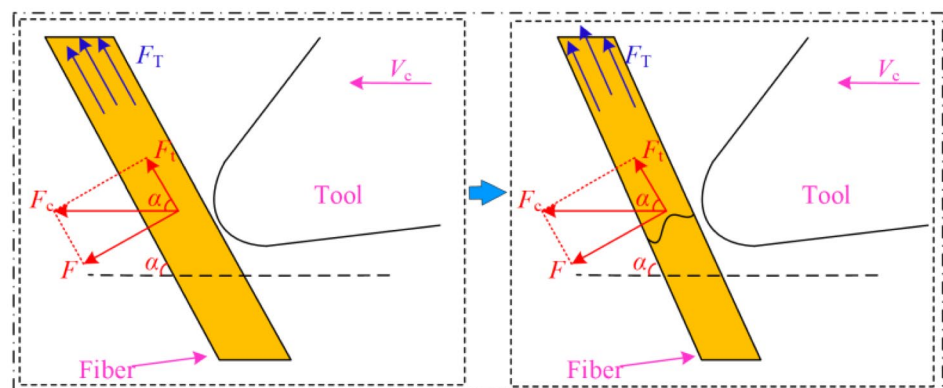
(b) Fiber breakage under tensile force

effectively reduced. Additionally, the tip of the micro-tooth structure is in the shape of a "hook tooth." The pulling effect on the fibers can be provided. The required tensile stress for the "pull-shear" removal principle can be applied on the fibers. However, due to the micro-tooth, the chip groove is too small. Therefore, the tool edges are wrapped by the Kevlar fibers, resulting in low efficiency and poor machining quality. To increase the chip removal space, two PCD straight edges are employed in the novel compound structure milling tool. The PCD milling tool with straight edges has large chip removal space, as depicted in Fig. 2. The novel compound structure milling tool is designed by these two existing tool structures. During the milling, the micro-tooth structure can effectively collect and pull the uncut the Kevlar fiber bundles. Subsequently, these uncut fiber bundles can be cut off by PCD blades using the "pull-shear" removal principle. Then, the Kevlar fibers can be completely cut off (Fig. 3).

3 Air flow modeling and cutting modeling

3.1 Air flow model for fibers removal

3.1.1 Theory of fibers suspension in fluid field

In order to analyze the burr and chip flow during the cutting movement of the novel compound structure milling tool, the cutting mechanism of fish-scale micro-tooth structure is studied. To verify whether the new compound structure milling tool can effectively achieve the fiber "pull-cut" removal effect, the air flow model is modeled for analyzing the fibers

removal. Therefore, the chip flow field in the cutting process of novel compound structure milling tool is analyzed.

First of all, it is necessary to determine the suspension conditions of furry and chips, and equivalent to calculate the irregular furry and chip size. Then, the suspension velocity of different volumes of chips in the air is analyzed and calculated.

(1) Chip equivalent method

Observed by electron microscope, the types of chips include the long burrs, curly sphere chips, and chunk chips, as investigated in Fig. 4. The minimum size of the burrs is 14 μm; the maximum size of these chips is 524 μm. In order to simulate the real state of the cutting process of the fibers as closely as possible and simplify the calculation as much as possible, the fiber is approximately equivalent to massless air and the air is simulated as a sphere of the same volume.

(2) Calculation of suspension velocity

Taking equivalent spherical particles as the main analysis object, the force diagram is illustrated in Fig. 5. The air resistance is F_R; the floating weight is W_S. The mechanical equilibrium conditions at this time can be expressed as Eq. (1) [29].

$$\begin{cases} F_R = C\frac{\pi}{4}d_s^2 r\rho\frac{v^2}{2} \\ W_s = \frac{\rho}{6}d_s^3(r_s - r)g \end{cases} \tag{1}$$

The simplified free-suspension velocity of a sphere in the air can be written as follows:

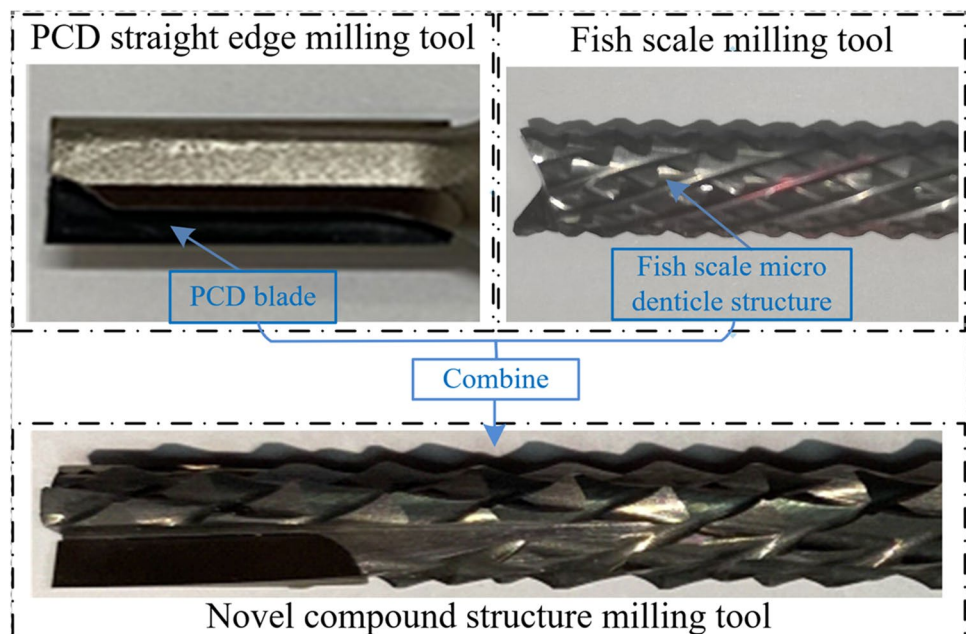**Fig. 2** The design idea of the novel compound structure milling tool

PCD straight edge milling tool

Fish scale milling tool

PCD blade

Fish scale micro denticle structure

Combine

Novel compound structure milling tool

Fig. 3 The principle of "pull-shear" action of the novel compound structure milling tool
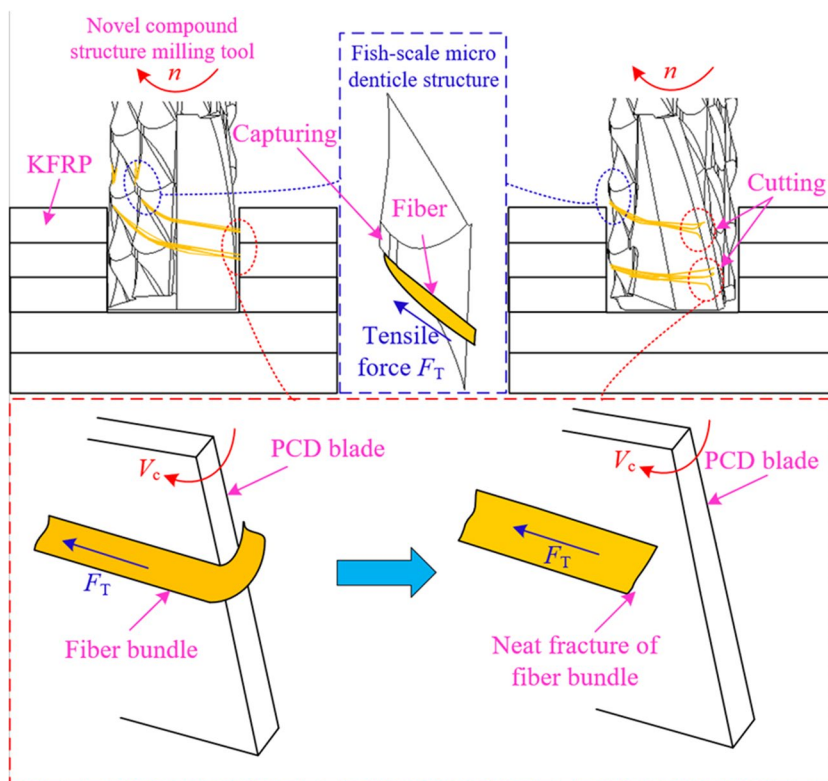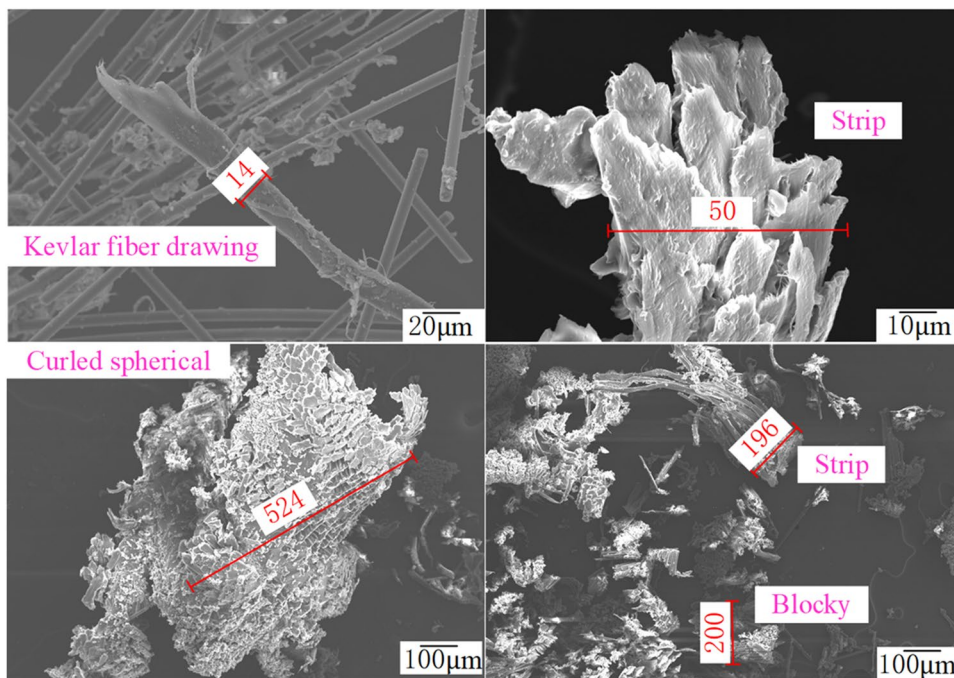

Fig. 4 Chip type and size

$$v_0 = \sqrt{\frac{4g}{3} \frac{d_s(\rho_s - \rho)}{C\rho}} \qquad (2)$$

where v_0 is the free-suspension velocity of the sphere, d_s is the diameter of the sphere, ρ is the air density, ρ_s is the

material density, C is the drag coefficient, and g is the gravitational acceleration, respectively.

The drag coefficient C of a sphere in the fluid can be determined by the Reynolds number R_e of the moving body. Here, R_e can be determined by fluid state. Nevertheless, the fluid states have different dominant resistance properties. The fluid
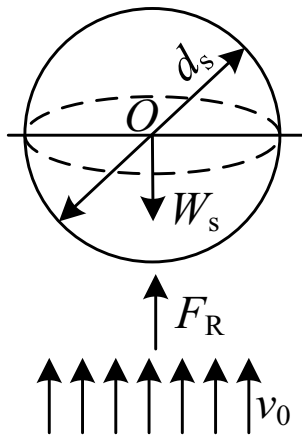
Fig. 5 Mechanical equilibrium condition of particle suspension

$$C = \frac{24}{R_e} = \frac{24\mu}{v_0 d_s \rho} \tag{3}$$

Here, the suspension velocity (v_0) and adaptation diameter (d_s) can be rewritten by Eq. (4):

$$\begin{cases} v_0 = \frac{d_s^2(\rho_s-\rho)g}{18\mu} \\ d_s \leq 1.225\left[\frac{\mu^2}{\rho(\rho_s-\rho)}\right]^{\frac{1}{3}} \end{cases} \tag{4}$$

where μ is the aerodynamic viscosity coefficient. The suitable diameter $d_s \leq 72.09$ μm can be obtained by the air density, the fiber furry density, and aerodynamic viscosity coefficient. When the adaptive diameter reaches the maximum, the suspension velocity v_0 is equal to 0.21 m/s.

state is mainly divided into the flow around state, the vortex state and the transitional state, respectively. Actually, the transitional state is the fluid state between the flow around state and the vortex state. Then, the key parameters of these three fluid states can be expressed as follows.

1. When the suspended body is in the flow around state, with Reynolds number (R_e) ≤ 1, the drag coefficient (C) can be calculated as follows:

2. When the suspended body is in the turbulent flow state, as the Reynolds number (R_e) ranging from 500 to 2×10^5, the drag coefficient (C) can be derived as 0.44. Thus, the suspended velocity and the corresponding diameter can be calculated as follows:

$$\begin{cases} v_0 = 5.45\sqrt{\frac{d_s(\rho_s-\rho)}{\rho}} \\ 20.4\left[\frac{\mu^2}{\rho(\rho_s-\rho)}\right]^{\frac{1}{3}} \leq d_s \leq 1100\left[\frac{\mu^2}{\rho(\rho_s-\rho)}\right]^{\frac{1}{3}} \end{cases} \tag{5}$$

Similarly, the corresponding diameter can be determined within the range of 1.2 mm $\leq d_s \leq$ 6.47 mm.

Fig. 6 Fluid domain simulation model

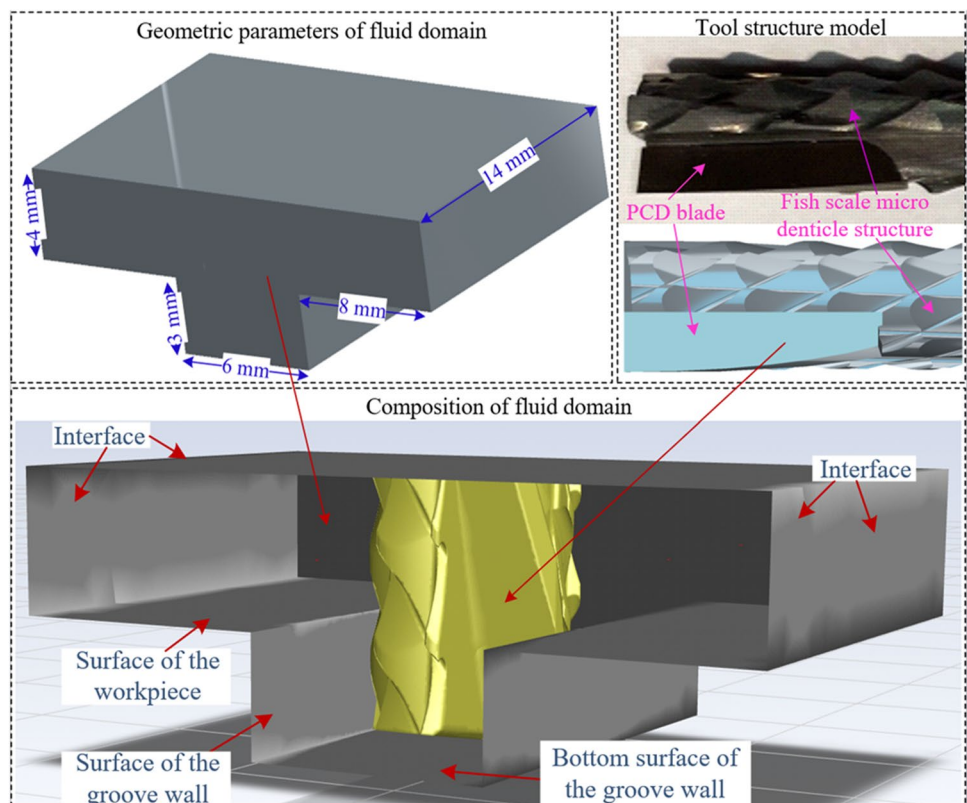**Table 1** Setting of boundary conditions for flow simulation

Items	Setting	Value
The entrance of the flow channel	Velocity inlet boundary	420 mm/min
The exit of the flow channel	Pressure outlet boundary	0 Pa (relative to atmospheric pressure)
Acceleration of gravity	Rotational slip condition	4000 rpm

Hence, the suspended velocity varies from $6.40 \text{ m/s} \leq v_0 \leq 14.83 \text{ m/s}$.

3. When the suspended body is in the transitional state, as the Reynolds number (R_e) ranging from 5.8 to 500, the drag coefficient (C) can be given as follows:

$$C = \frac{10}{\sqrt{R_e}} = \frac{10\sqrt{\mu}}{\sqrt{v_0 d_s \rho}} \tag{6}$$

The suspension velocity (v_0) and adaptation diameter (d_s) can be calculated as follows:

$$\begin{cases} v_0 = 1.195 d_s \left[\frac{(\rho_s - \rho)^2}{\rho \mu} \right]^{\frac{1}{3}} \\ 2.2 \left[\frac{\mu^2}{\rho(\rho_s - \rho)} \right]^{\frac{1}{3}} \leq d_s \leq 20.4 \left[\frac{\mu^2}{\rho(\rho_s - \rho)} \right]^{\frac{1}{3}} \end{cases} \tag{7}$$

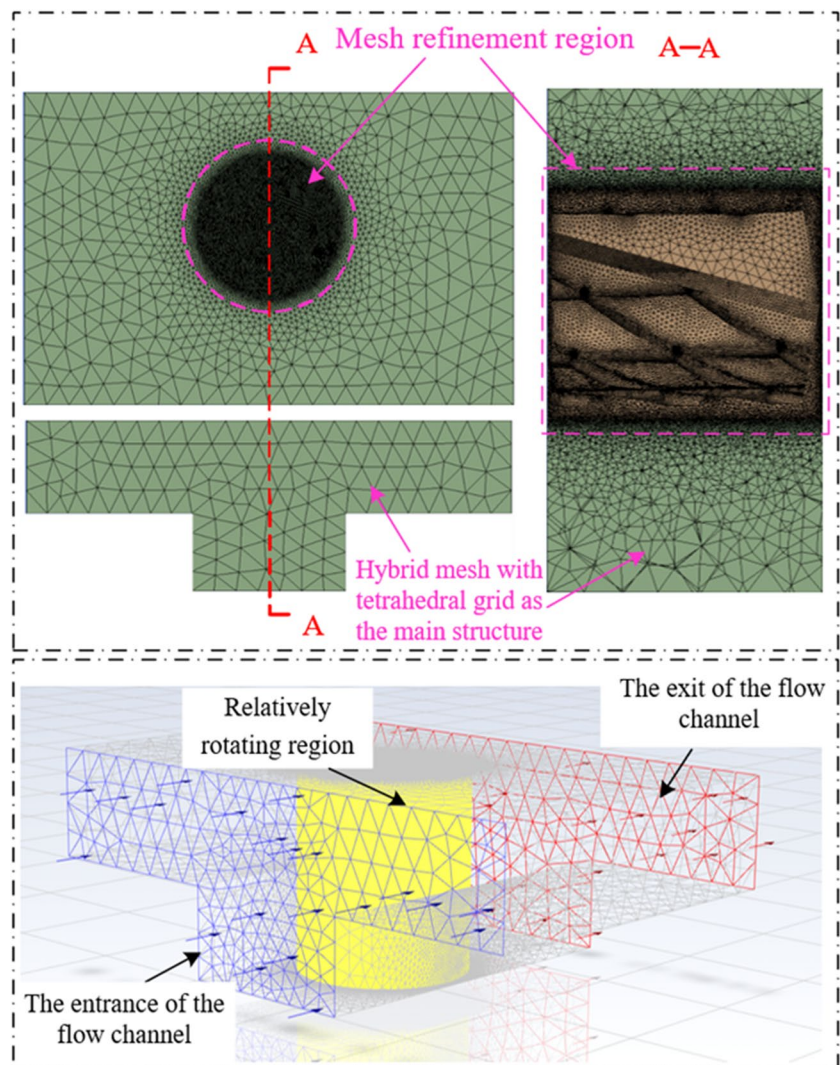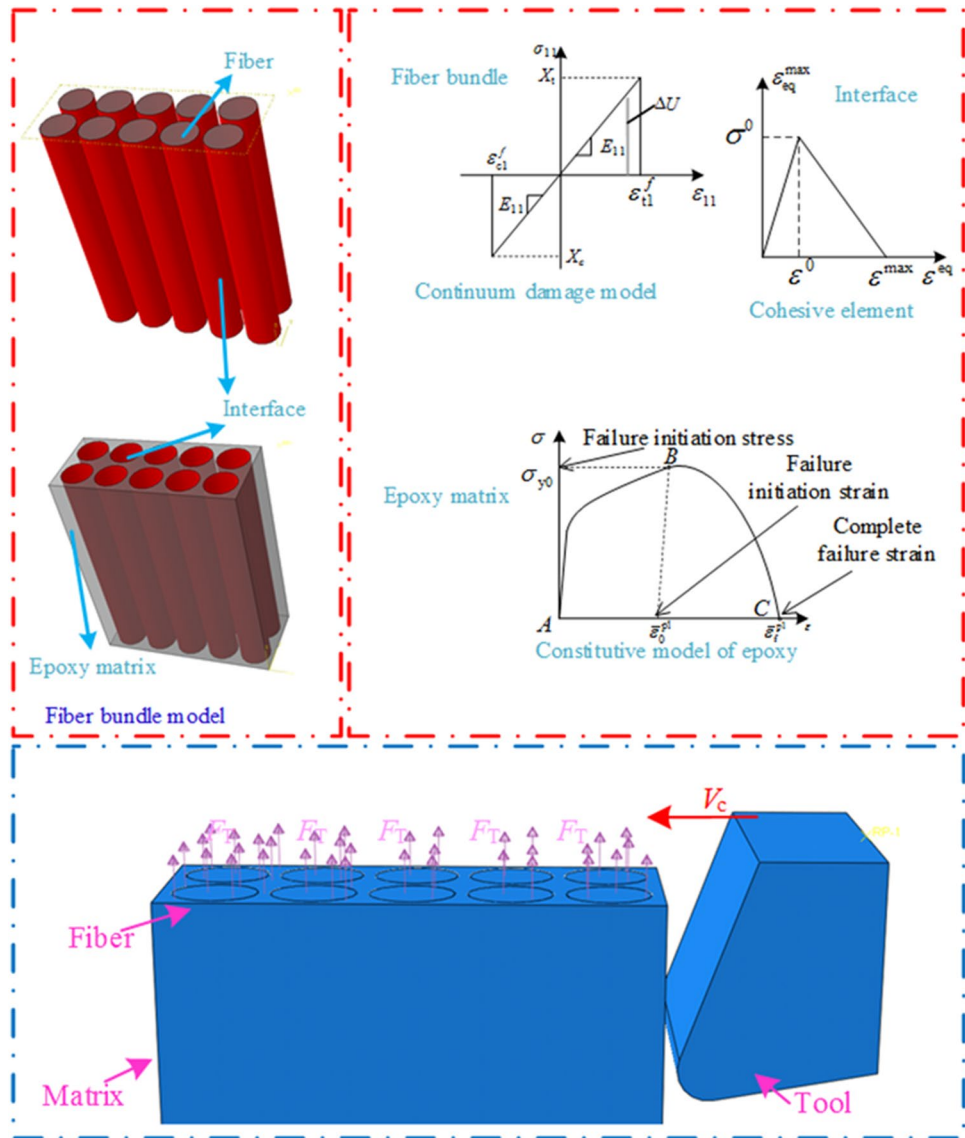**Fig. 7** Mesh model and fluid boundary condition

Fig. 8 Finite element cutting model and the constitutive definition of FEM modeling

The suitable diameter can be estimated as 129.4 μm $\leq d_s \leq$ 1.2 mm. The suspension velocity is 0.68 m/s $\leq v_0 \leq$ 6.33 m/s.

3.1.2 Modeling for fibers flow state during compound structure tool milling

After determining the suspension conditions of the furry and chips in the air, the flow field simulations of the flow velocity during the milling process of the novel compound structure milling tool are established. The "pull-cut" removal effectiveness of the tool and the flow states of the fibers are verified.

The fluid domain geometry model consists of two parts, i.e., the air basin and the tool. In the actual cutting process, the flow field state near the tool is analyzed emphatically,

due to the main area affected by air flow is near the tool. In order to simplify the model, the tool is placed in a prefabricated groove. The air flow state is analyzed when the tool is rotating at high speed, as displayed in Fig. 6. The geometric model of the workpiece is built in ANSYS. The fluid domain in the air area above the groove and the workpiece surface nearby is established. The geometric model of the tool is established by Pro/E software with reference to the actual tool. The air area in the tool zone is replaced by the tool.

Table 2 Mesh settings

Items	Mesh type	Mesh size
Fiber	C3D8R	1.7 μm
Resin matrix	C3D8R	5 μm
Tool	C3D4	7 μm

Table 3 Properties of KFRP

Items	Value
Fiber elastic modulus	$E_1 = 22$ GPa, $E_2 = E_3 = 9$ GPa
Fiber Poisson ratio	$\nu_{12} = \nu_{13} = 0.25$, $\nu_{23} = 0.33$
Fiber shear modulus	$G_{12} = G_{13} = 2.7$ GPa
Fiber tensile strength	$X_t = 0.55$ GPa
Fiber compressive strength	$X_c = 0.28$ GPa
Matrix elastic modulus	$\nu = 0.4$
Matrix Poisson ratio	$\sigma_{y0} = 74.4$ MPa
Interface properties	$t0\ n = 60$ MPa, $t0\ s = t0\ t = 110$ MPa
	$Gc\ n = 0.33$ (N/mm^2), $Gs\ c = Gc\ t = 1.209$ (N/mm^2)
	$K_{nn} = 4 \times 10^6$ (N/mm^2), $K_{ss} = K_{tt} = 1 \times 10^6$ (N/mm^2)

Table 4 Properties of tool

Items		Value
YG6X	Specific heat capacity	224 (KJ/kg·°C)
	Heat conductivity coefficient	79.6 W/(m·K)
PCD	Specific heat capacity	653 (KJ/kg·°C)
	Heat conductivity coefficient	700 W/(m·K)
Tool rake angle		20°
Tool clearance angle		5°
Tool blunt round radius		10 μm

Table 6 Milling parameters

$V_c = 64$ m/min; $a_p = 3$ mm	V_f (mm/min)			
	100	260	420	580
$V_c = 79$ m/min; $a_p = 3$ mm	V_f (mm/min)			
	100	260	420	580
$V_c = 94$ m/min; $a_p = 3$ mm	V_f (mm/min)			
	100	260	420	580
$V_c = 109$ m/min; $a_p = 3$ mm	V_f (mm/min)			
	100	260	420	580
$V_c = 64$ m/min; $V_f = 260$ mm/min	a_p (mm)			
	1	2	3	4

So as to carefully analyze the airflow velocity around the tool, the mesh area needs to be set up reasonably. The mesh of the air area around the tool is refined and the boundary conditions are set. ANSYS mesh component is used to mesh the parts, i.e., the tool, workpiece, and air domain. The structured hybrid mesh is used for the air domain. The "SIZE FUNCTION" component is applied to refine the air area mesh on the tool surface.

Subsequently, the meshed model is imported into "Fluent" module. The turbulence model is built by RNGk-ε simulation method. Then, the turbulence simulation is operated by the second-order implicit propulsion method. In order to simulate the feed velocity of the air flow relative to the tool during feeding, the flow velocity is set at the entrance of the flow channel. The negative pressure environment is set at the exit of the flow channel. The other four surfaces of the flow channel are set as standard wall. The tool standard wall is set as "relative sliding" mode. The settings of boundary conditions for flow simulation are shown in Table 1.

The four sides and the tool are set to the standard wall, the tool wall is set to the relative sliding, and the other walls are set to the standard wall. The rotary slip condition is set in the tool critical area, and the relative motion reference area is set to the air domain, as shown in Fig. 7. According to the above settings, the transient characteristics of the air domain in the milling process are described by simulation analysis, and the flow of chips with air in the milling process is calculated and analyzed.

3.2 Finite element modeling for cutting fibers

So as to further analyze the cutting state of Kevlar fiber in the process of "pull-shear" removal, the finite element cutting model of Kevlar fiber composite is constructed. Since KFRP consists of Kevlar fibers and epoxy resin matrix. The strength limits of the fibers and matrix differ greatly. In order to accurately simulate the failure behavior of KFRP during the cutting process, the geometric model of the cutter-workpiece is built. The material properties and their damage criteria are defined separately. The cutting simulation

Table 5 Fluid related main parameters

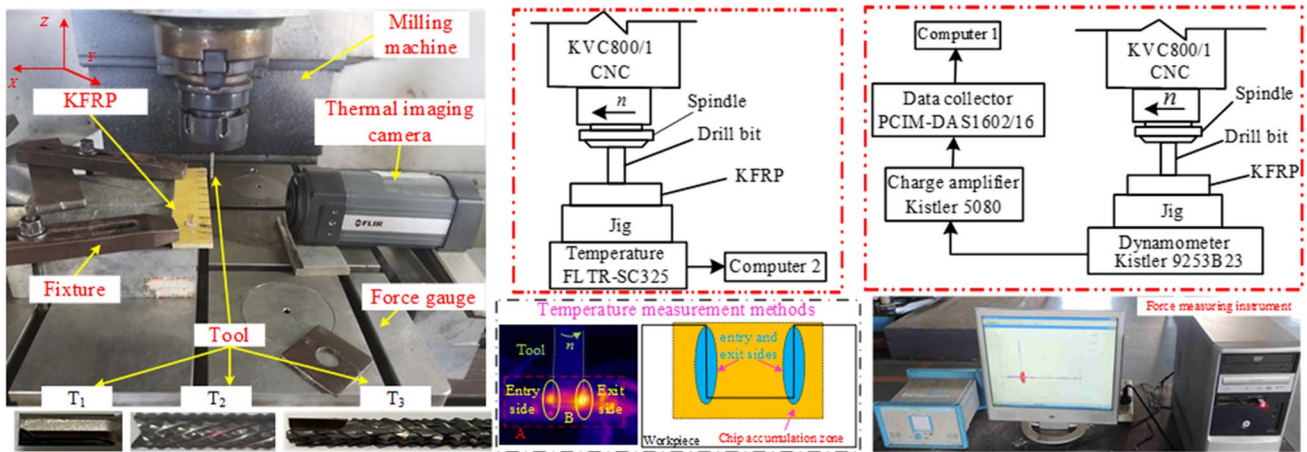| Items	Symbol	Value
Kevlar fiber density	ρ_s	1380 kg/m^3
Air density	ρ	1.205 kg/m^3
Aerodynamic viscosity coefficient	μ	1.84×10^{-5} Pa·s
Acceleration of gravity	g	9.8 m/s^2

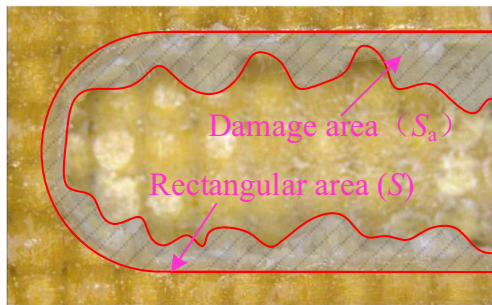**Fig. 9** Experimental setups and the measurement systems

Fig. 10 Defect factor definition

is carried out in the microscopic model at a typical fiber angle of 90° to study the fiber damage form, as illustrated in Fig. 8. In the microscopic cutting model, the tool is bound to the rigid body C3D4. The bottom and sides of the material are fixed. The hexahedral mesh is generated by scanning a single fiber along the fiber axis direction using the central axis algorithm. The cell type is set as C3D8R. The cell size of the mesh is set to 1.7 μm.

The finite element cutting simulation model was used to analyze the cutting effect with and without tension. Then, the validity of the "pull-shear" removal principle is verified. Here, the cutting simulation with the typical angle of 90° is only considered. The geometric size of the resin matrix model is 34 μm × 82 μm × 150 μm. The Kevlar fibers are evenly inserted into the resin matrix model at 2 × 5, as shown in Fig. 8. In the microscopic cutting model, the tool is bound to a rigid body. The bottom and sides of the material are fixed. The hexahedral mesh is generated by scanning a single fiber along the fiber axis direction using the central axis algorithm. The mash settings of each part are shown in Table 2.

The constitutive relation of fibers is developed and realized by VUMAT. The fibers are defined as transversely isotropic elastic materials. The maximum stress failure criterion is adopted for simulating the fracture failure of the fibers. The stress-strain relationship of the fiber element under axial tension or compression is depicted in Fig. 8. When the maximum axial principal stress of the fiber element reaches the ultimate tensile strength (X_t) of the fiber or the minimum principal stress reaches the ultimate compressive strength (X_c) of the fiber, the fiber element will fail and be deleted. The epoxy resin is defined as isotropic elastoplastic material in this model. The shear failure criterion is adopted as the initial failure criterion for the epoxy resin. In Fig. 8, the segment A-B is the response curve when the material does not fail. The point B is the initial damage point of the material. The segment B-C is the damage evolution curve of the material. KFRP is usually a laminated structure. Then, a zero-thickness cohesive force unit is used as the interface. The tractor-separation viscous material model is adopted for the interface. When the initial damage condition is satisfied, the unit will be damaged and expanded under cutting load. At this time, the stratification occurs and the stiffness begins to decrease linearly.

4 Experimental procedures

4.1 Experimental material and milling tool

The material used in the experiment is plain woven Kevlar fiber-reinforced polymer (K49/Epoxy), and its performance parameters were shown in Table 3. The fiber volume fraction is 60 vol%, the diameter of a single fiber is about 12 μm, single layer thickness is 0.33 mm, and plate thickness is 5 mm.
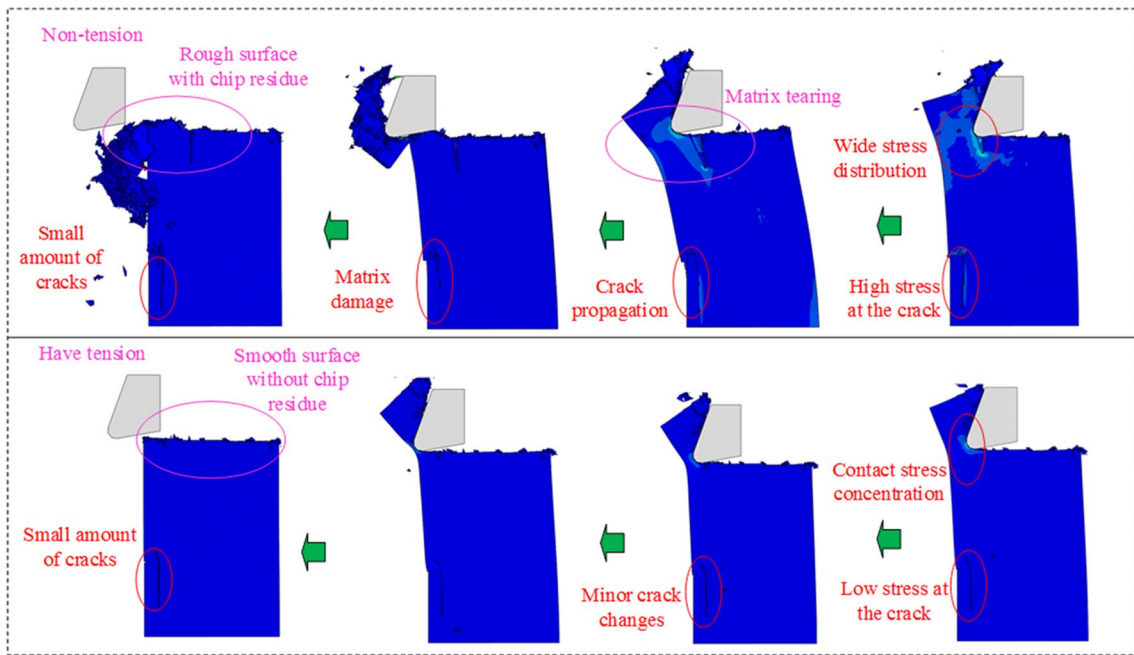
(a) The surface quality of the material with or without tension
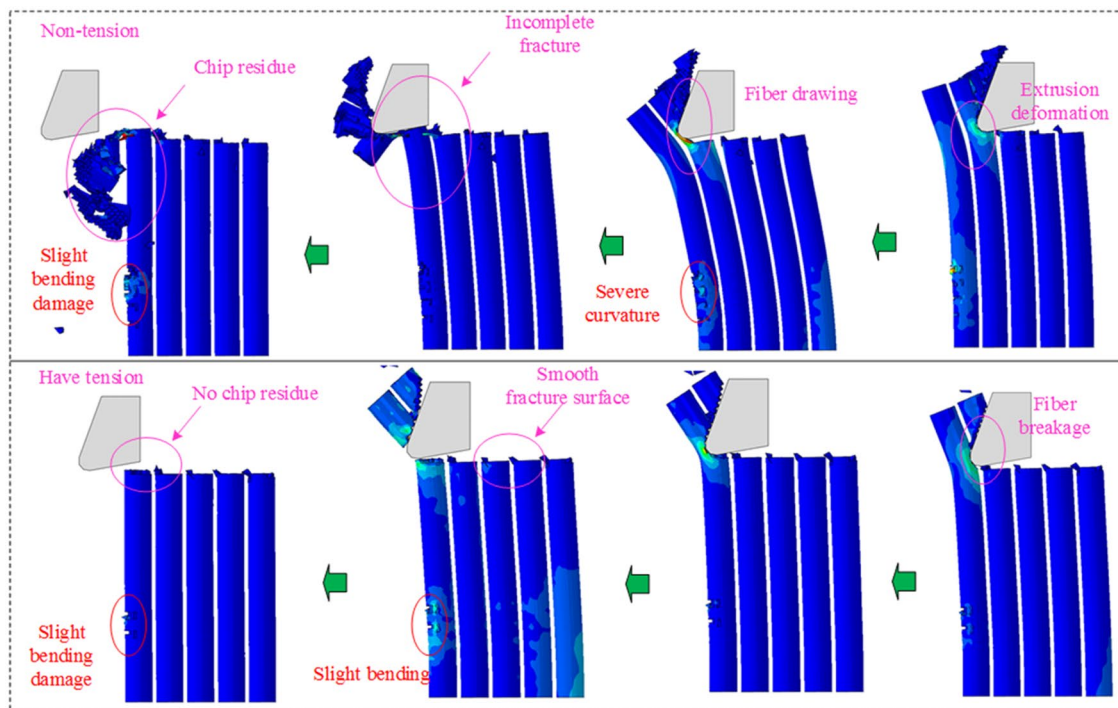
(b) Breakage of fibers with or without tensile force

Fig. 11 Simulation comparison with and without tension

In order to analyze the cutting effect of the novel compound tool designed by the "pull-shear" cutting principle, three tools (e.g., PCD straight edge milling tool (T_1), fish-scale milling tool (T_2), novel compound structure milling tool (T_3)) were employed in the tests, as displayed in Fig. 2.

The T_1 is divided into two parts: the PCD blade and the cemented carbide handle. T_2 is made of cemented carbide. The cutting edge is composed of some small cutting edges with different turning directions. T_3 is composed of two PCD blades and a few of fish-scale micro-tooth structure cutter.
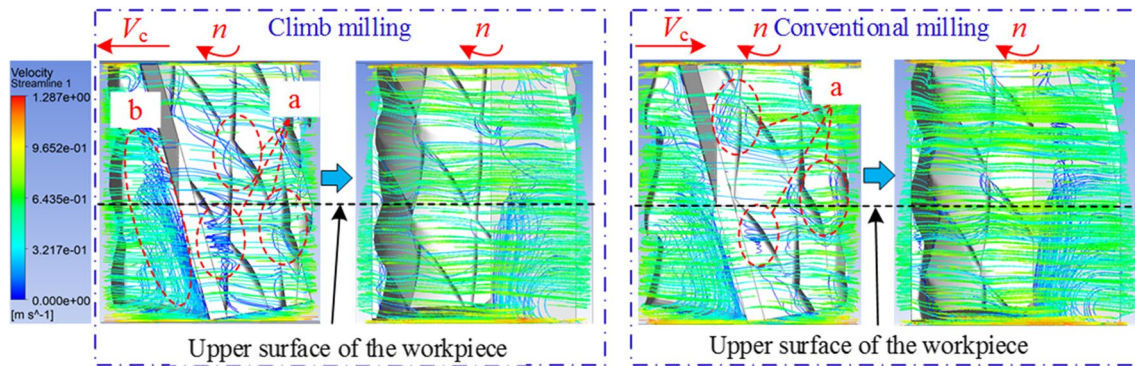
Fig. 12 Steady state of air flow

All the tool diameters are 6 mm. The properties of tool were presented in Table 4.

The parameters used for air flow model were displayed in Table 5.

4.2 Experimental details

In order to study the influence of milling parameters on the KFRP milling effect by using the existing tool and T_3, a series of KFRP groove milling experiments were designed. These experiments were carried out on KVC1050M vertical machining center without cooling and with the cutting speed of 64~109 m/min (i.e., 64, 79, 94, 109 m/min), the feed speed of 100~580 mm/min (i.e., 100, 260, 420, 580 m/min), and the cutting depth of 1~4 mm (i.e., 1, 2, 3, 4 mm), respectively. The test parameters are shown in Table 6.

All the experimental setups and the force and temperature measurement systems were illustrated in Fig. 9.

4.3 The type of machining defect and the evaluation method of machining quality

Defects such as burr, furry, and delamination are easy to occur in the processing of Kevlar composite materials. The appearance of these defects not only affects the dimensional accuracy of parts processing, but also restricts the subsequent assembly of products and the performance of components. Therefore, in order to be able to accurately judge the processing quality of materials and provide data standards for subsequent analysis, burr defect factor K is used as the evaluation index of milling processing, as shown in Fig. 10. The ratio of the damage area S_a to the slot area S was used as the burr defect factor. The S_a is the area occupied by the defect. The slot area S is the area of the milled slot. The damaged area S_a and the milling groove area S were measured by

the microscopy and image processing software. The relevant calculation formula is shown in Eq. (8).

$$K = \frac{S_a}{S} \tag{8}$$

5 Results and discussion

5.1 Fiber "pull-shear" principle finite element cutting simulation analysis

The comparison of microscopic cutting surfaces is reported in Fig. 11. When the fibers are subjected to the tensile force, the cutting surface is neat, with fewer cracks at the boundary. When the fibers are not subjected to the tensile force, the cutting surface is rough, with a lot of burrs. The matrix has multiple cracks. The cutting effect is obviously poor.

While the fiber without tension, the fiber will bend and stretch as the tool contacts the fiber, as shown in Fig. 11a. When the tensile strength is exceeded, the fibers ductile fracture will occur. The fracture point is above the contact point with severe fiber bending damage at the boundary. The fibers in the final position are not completely removed. The overall fiber fracture is rough with a large number of burrs. Under the action of tension, the bending deformation of the fiber is reduced. Shear fracture occurs before tensile fracture of the fiber. Additionally, the fracture point is flush with the tool contact point. The fiber curvature at the boundary is reduced. The whole fiber fracture is smooth. In Fig. 11b, the breakage of fibers under the action of tension or no can be clearly compared. Therefore, when the fibers are subjected to tension, the cutting surface quality is significantly improved. Noteworthy, the "pull-shear" removal principle can be implemented effectively. The fibers can be effectively cut off in time.

(a) Different feed speed

(b) Different cutting speed

(c) Different tool structure

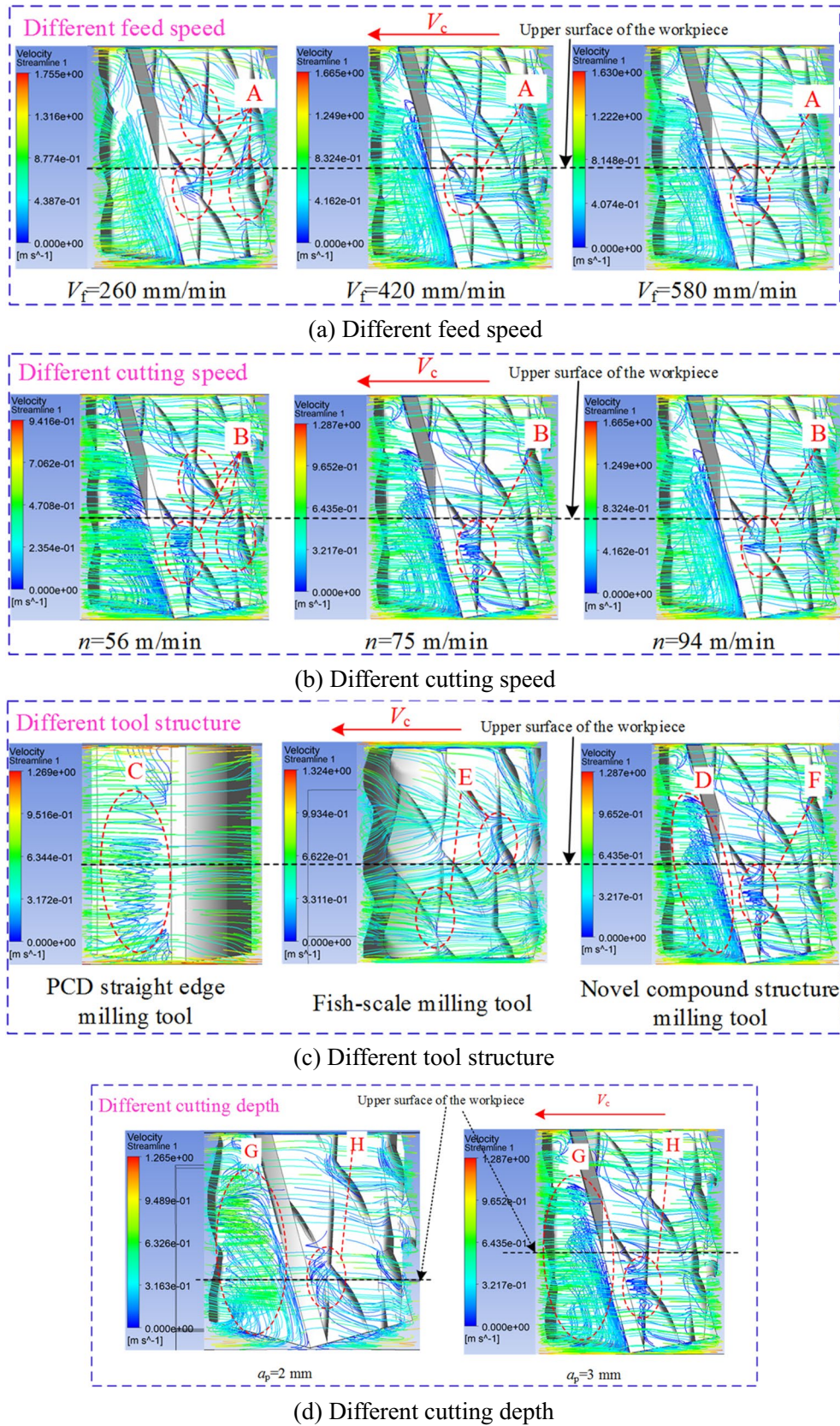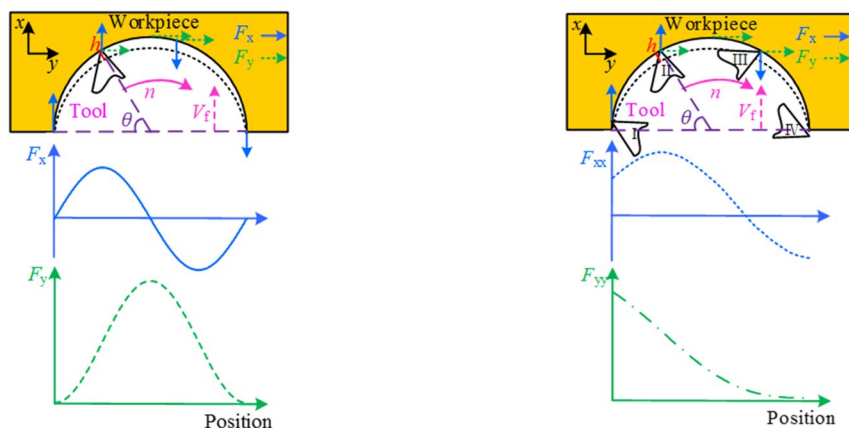(d) Different cutting depth

Fig. 13 The influence of machining parameters on flow velocity

(a) Trend of single-edge cutting force variation in tool milling process

(b) Trend of multi-edge cutting force variation in tool milling process

Fig. 14 Change trend of the cutting force during tool milling

5.2 Simulation analysis of fiber flow state in cutting with the compound structure milling tool

The flow of the residual chips and furry in the milling process of T_3 is analyzed when the feed speed $V_f = 420$ mm/min, cutting speed $V_f = 75$ m/min, and cutting depth $a_p = 3$ mm.

According to the fiber suspension theory in Section 3.1.1, the suspension conditions of chips and furry were determined, and whether the chips and furry could move with the air flow was judged. In the simulation results of flow field, different color velocity vector lines represent different airflow velocity, where the blue velocity vector line represents the lower airflow velocity. When the chips and furry move to the position of the blue line with the air flow, the chips and furry cannot reach the suspension velocity. So low speed stagnation occurs; the chips and furry are caught in the micro-tooth structure of the tool. The flow field simulation results are analyzed as follows: At a certain stable moment in the cutting process of the tool, the flow velocity distribution vector around the tool is shown in Fig. 12. It can be seen that the flow velocity around the tool is mostly between 0.322 and 0.965 m/s. It can be observed that when the chips move with the air flow to the micro-tooth structure, the low-speed stagnation occurs in many places (e.g., a in Fig. 12). This phenomenon exists in both up-milling and down-milling. The stagnation effect of down-milling is stronger than that of up-milling at the same height. When the chips and furry reach near the micro-tooth, the residual chips and the furry can be hooked, then the "pull" effect can be achieved. After the residual chips and the furry are hooked, the residual chips and the furry can be cut off instantaneously by the PCD blades, then the "shear" effect can be achieved. The excised chips strand in front of the PCD blade with the air flow (e.g., b in Fig. 12). With the cutting movement of the tool, the

excised chips can be continued to accumulate and discharged when the excised chips are squeezed to the upper surface of the workpiece. During the milling, the "pull-shear" effect of T_3 can be verified. To consider the effect of different machining parameters on the flow rate around the tool, the influences of different machining parameters on the flow velocity around T_3 in the down-milling state are investigated.

When the cutting speed $V_c = 94$ m/min (viz., spindle speed $n = 5000$ r/min) and the cutting depth $a_p = 3$ mm, the air velocity decreases gradually with the increase of feed speed, as presented in Fig. 13a. The air velocity decreases from 1.316 to 1.222 m/s. This means that the maximum value of the suspended fiber equivalent diameter d_s decreases from 249 to 231 μm. The difference value of this maximum equivalent diameter is only 18 μm. This is similar to the size of a Kevlar fiber. Thus, the effect on the "pull-shear" removal effect is small. The air flow lines gradually densify with the increase of feed speed (e.g., A in Fig. 13a). To comprehensively analyze the above results, the residence effect of the fish-scale micro-tooth can be enhanced, indicating that the "pull-shear" removal effect increases as the feed speed increases.

When the feed speed $V_f = 420$ mm/min and the cutting depth $a_p = 3$ mm, the change of air flow velocity around the tool with the spindle speed is investigated in Fig. 13b. When the spindle speed is lower (e.g., $n \leq 4000$ r/min), the air flow lines nearby the micro-tooth is basically unchanged with the increasing of the spindle speed. At low spindle speed, the retention effect of the micro-tooth changes little with the increasing of the spindle speed. Nevertheless, when the cutting speed is higher (e.g., $V_c > 4000$ r/min), the air flow lines at the position of B in Fig. 13b reduce significantly with the increase of the cutting speed. Thus, the retention effect of micro-tooth decreases greatly with the increase of the spindle speeds at high cutting speed. The air flow velocity around the

Fig. 15 Typical cutting force curves ($V_c = 64$ m/min, $a_p = 3$ mm, $V_f = 260$ mm/min)
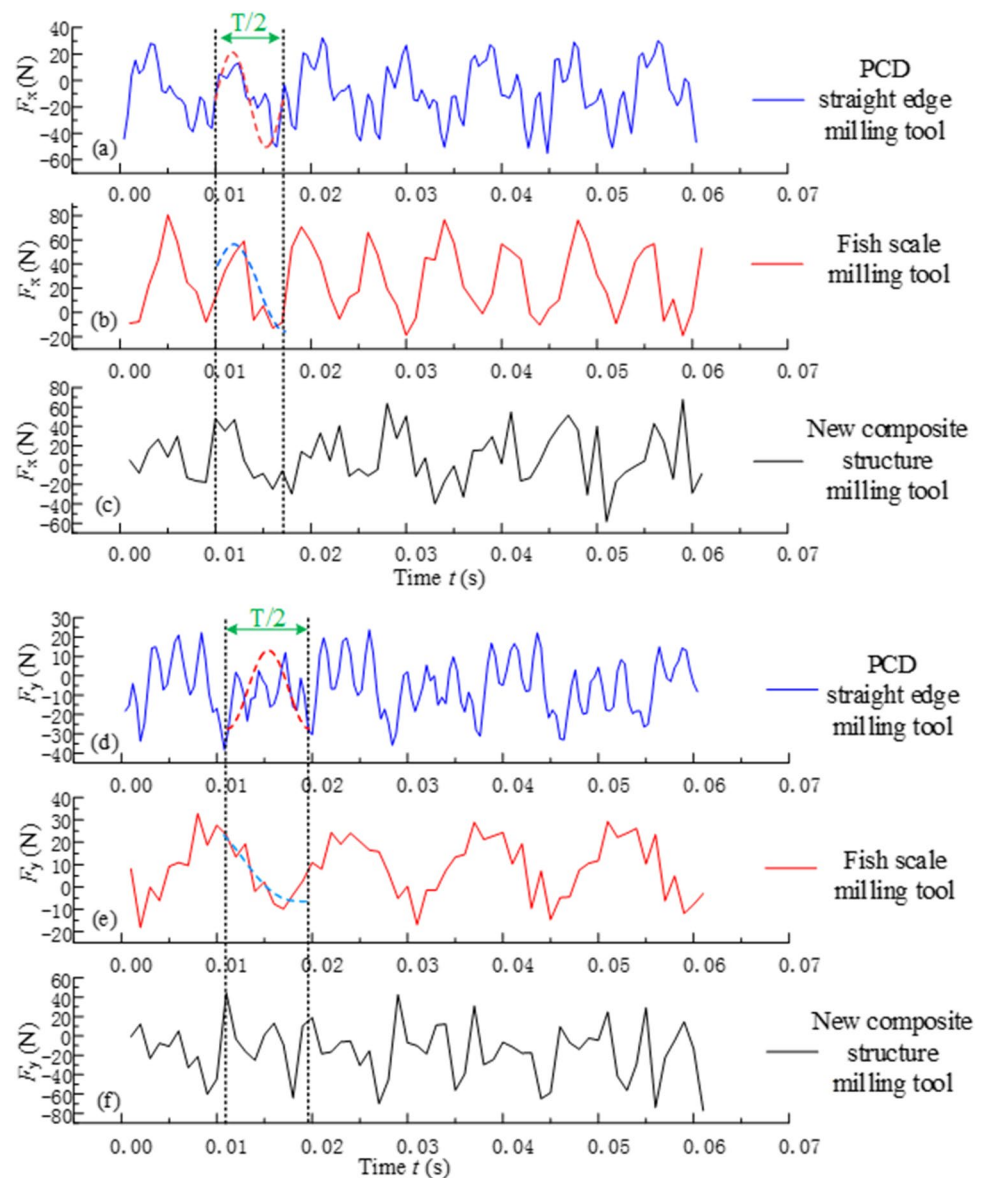
tool increases from 0.706 to 1.249 m/s with the increase of the cutting speed. The equivalent diameters of the residual chips and furry can be increased from 134 to 231 μm. Similarly, this means that the suspended fiber equivalent diameter significantly increases with the increasing of the cutting speed. In conclusion, the "pull-shear" removal effect is enhanced with the increase of the spindle speed at low spindle speed, but the pull-shear removal decreases with the increase of cutting speed at high spindle speed.

The cutting effects of T_1, T_2, and T_3 are analyzed under the same process parameters. In Fig. 13c, a large amount of air flow accumulates at the position of C and D. A low-speed stagnation of the air flow appears at E and F position. This indicates that the fish-scale micro-tooth can effectively stop the air flow at a low speed. Thus, the "pulling" effect can be realized for Kevlar

fibers. Compared to the conventional tools, the retention effect of the fish-scale micro-tooth of T_3 is the strongest.

The effect of the cutting depth on the air flow is analyzed, as displayed in Fig. 13d. Here, the cutting depth a_p is only selected as 2 mm and 3 mm, and the feed speed $V_f = 420$ mm/min and the cutting speed $V_c = 94$ m/min. The cutting depth has little effect on the air flow around the tool. The flow speed of the air in front of the PCD blades is different from in the fish-scale micro-tooth near the upper surface of the workpiece. When the cutting process at a larger cutting depth, the residual chips and the furry are easy to accumulate at the position of G in Fig. 13d. Then, the residual chips and the furry easily lead to the problem of heat dissipation. If the cutting process is at a lower cutting depth, the low-speed stagnation of the air flow effect will be weakened (e.g., at the position H in Fig. 13d).
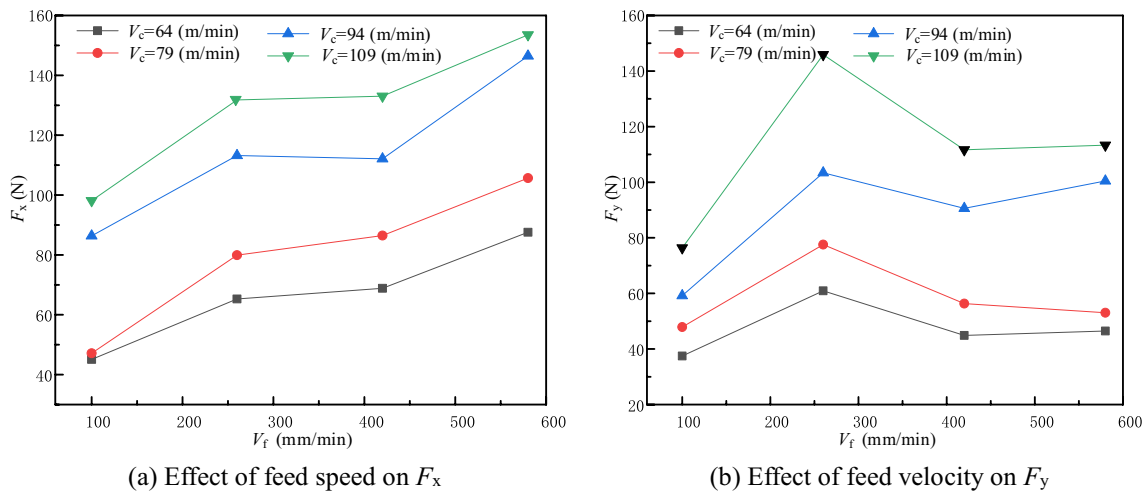
(a) Effect of feed speed on F_x (b) Effect of feed velocity on F_y

Fig. 16 Effect of the feed speed on the cutting forces ($a_p = 3$ mm)

Therefore, choosing an appropriate cutting depth has a positive influence on improving the machining quality of T_3.

In summary, the effect of T_3 on the retention of chips and furry is stronger than that of the conventional milling tool (e.g., T_1 and T_2). The feed speed has the greatest positively effect on T_3. The higher the cutting speed, the faster T_3 discharges chips, but the retention effect of the fish-scale structure on the chips and furry will be weakened. The cutting depth has also a great influence on T_3. When the cutting depth is large, the chips are easy to accumulate. When the cutting depth is small, the fish-scale micro-tooth involved in the cutting is reduced, affecting the "pulling-shearing" effect. Thus, the "pulling-shearing" effect can be effectively implemented by T_3. Nevertheless, the cutting parameters need to be selected suitable.

5.3 Experimental cutting force analysis of milling KFRP

5.3.1 Influence of different tool structures on cutting force

Generally, the characteristics of the milling forces are determined by the tool structure. Then, the characteristics of the milling forces of T_3 and the conventional tools are contrastively analyzed.

Theoretically, the single-edge cutting force can be estimated by cutting thickness h and feed per tooth f_z in different angular displacement θ, as expressed as Eq. (9). Furthermore, the X- and Y-direction single-edge and whole cutting forces (e.g., F_x, F_y, F_{xx}, F_{yy}) can be derived as Eq. (9).
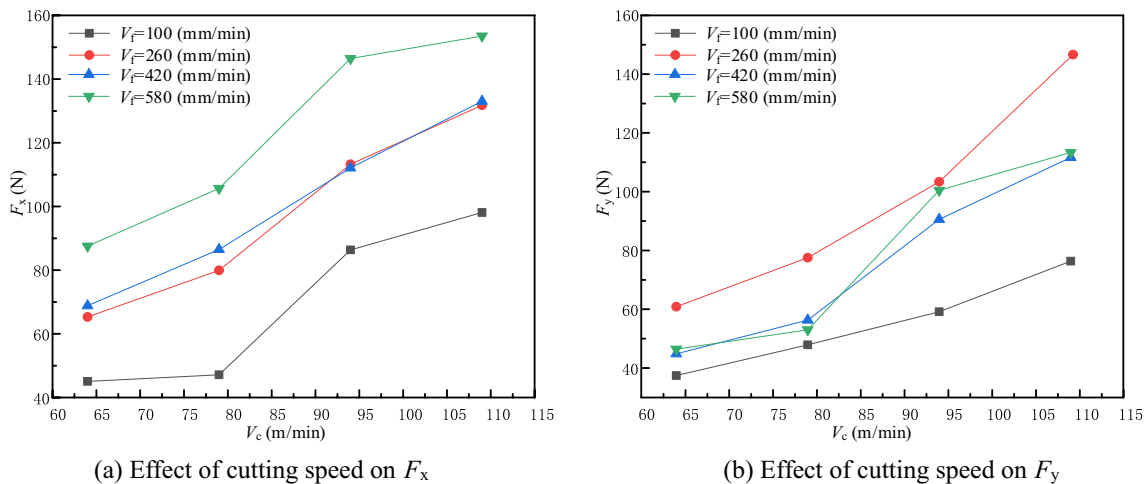

(a) Effect of cutting speed on F_x (b) Effect of cutting speed on F_y

Fig. 17 Effect of cutting speed on peak cutting force

$$
\begin{cases}
h = f_z \sin\theta \\
F_c = kh \\
F_x(\theta) = f_z k \sin\theta \cos\theta \\
F_y(\theta) = f_z k \sin\theta \sin\theta \\
F_{xx}(\theta) = \begin{cases} \sum\limits_{\theta=0}^{\pi}\sum\limits_{n=1}^{n} f_z k \sin\theta' \cos\theta' & \theta' \le \pi \\ 0 & \theta' > \pi \end{cases} \\
F_{yy}(\theta) = \begin{cases} \sum\limits_{\theta=0}^{\pi}\sum\limits_{n=1}^{n} f_z k \sin\theta' \sin\theta' & \theta' \le \pi \\ 0 & \theta' > \pi \end{cases}
\end{cases}
\tag{9}
$$

where $\theta' = \theta + (n-1)\cdot d$, n is the number of blades, θ is angular displacement, h is cutting thickness, f_z is feed per tooth, k is the cutting force per unit thickness, F_x is the feed force, and F_y is the tangential force.

T_1 consists of two blades cutter and T_2 consists of a lot of blades cutter. The structure of T_3 is combined with these two conventional tool structures. Therefore, the characteristics of the single-edge and multi-edges cutting forces in a period are carefully analyzed, as illustrated in Fig. 14.

The typical cutting force curves of these three tools (i.e., T_1, T_2, and T_3) are presented in Fig. 15. The characteristics of the typical cutting force curves can be summed up. Actually, the cutting forces of T_3 in a half cycle are superimposed by the other tool cutting forces.
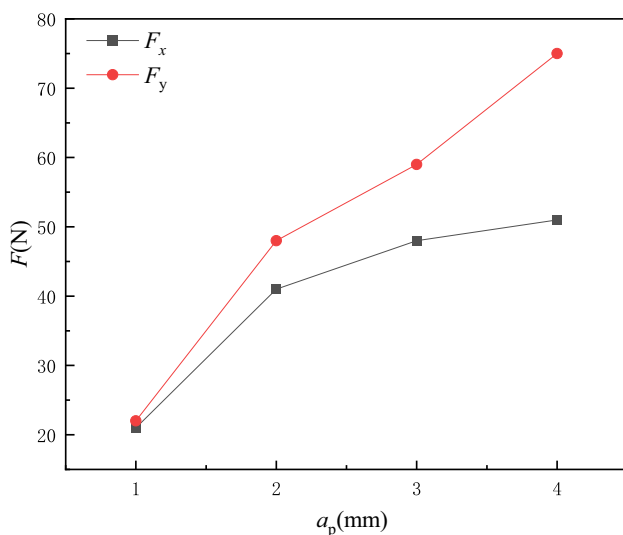

Fig. 18 Effect of cutting depth on peak cutting force ($V_c = 79$ m/min, $V_f = 260$ mm/min)

5.3.2 Influence of different machining parameters on cutting force

To analyze T_3 changes of the cutting forces with the milling parameters, the forces mean of maximum are investigated, as shown in Figs. 16, 17, and 18.

The feed force F_x overall increases with the increase of feed speed, as shown in Fig. 16a. When the cutting speed is 64 m/min, 79 m/min, 94 m/min, and 109 m/min and the feed speed is in the range of 100~580 mm/min, the feed force F_x increases by 42 N, 57 N, 61 N, and 55 N, respectively. The feed force F_x increases with the increase of feed speed when the cutting speed is constant. With the increase of feed speed, F_y presents an "augment-decrease-increase" fluctuation, as illustrated in Fig. 16b. When the feed speed is 260 mm/min, the maximum values reteach as 145 N, 104 N, 78 N, and 61 N, respectively.

With the increase of cutting speed, F_x and F_y both show an increasing trend, as displayed in Fig. 17. When the feed speed is 100 mm/min and the cutting speed is from 64 to 110 m/min, F_x increases from 46 to 97 N, and F_y increases by 37 N. When the feed speed is 260 mm/min and the cutting speed is from 64 to 110 m/min, F_x increases from 66 to 132 N, and F_y increases from 61 to 148 N. When the feed speed is 420 mm/min and the cutting speed is from 64 to 110 m/min, F_x increases from 69 to 133 N and F_y increases from 46 to 111 N. When the feed speed is 580 mm/min and the cutting speed is from 64 to 110 m/min, F_x increases from 88 to 153 N, and F_y increases from 46 to 111 N. When the cutting speed increases, the contact between the tool micro-tooth structure and the material increases. Increased friction leads to increased resistance, so the cutting force increases.

As can be seen from Fig. 18, F_x and F_y significantly increase with the increase of the cutting depth. As the cutting depth increases from 1 to 4 mm, F_x increases from 21 to 51 N and F_y increases from 22 to 75 N.
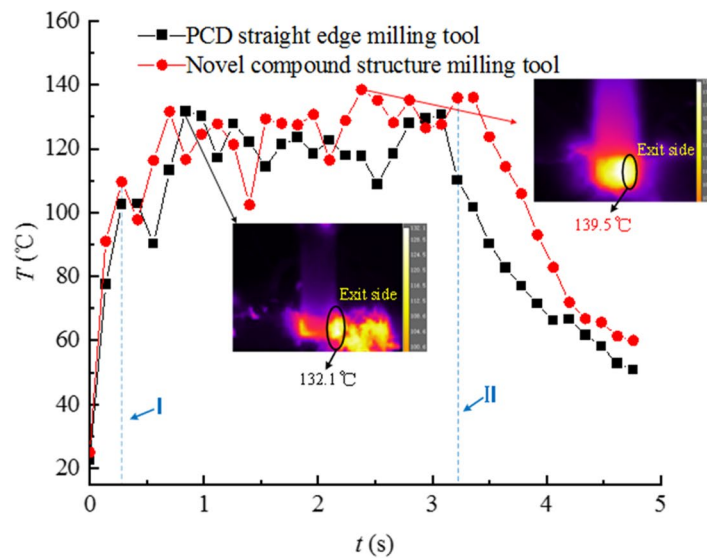
5.4 Analysis of time-varying characteristics and rules of temperature

Because the Kevlar fibers are difficult to be cut off by using T_2, a lot of furry defects occur during the milling processing. The machining process of this tool is covered by the uncut fibers, resulting in inaccurate temperature measurements. Therefore, the temperature variation of T_2 is not discussed in this study. Under the processing parameters of cutting speed 64 m/min, cutting depth 3 mm, and feed speed 260 mm/min, the processing tests were carried out with T_1 and T_3.

As the tool begins to process the material, the cutting temperature rises rapidly. The temperature of the cut exit side area is higher during the processing. So the temperature

of the cut exit side of the two tools is mainly analyzed, in this study. The temperature change of the cut exit side over time is shown in Fig. 19. At the beginning of machining, the cutting thickness gradually increases with the feed of the tool. At the same time, the cutting temperatures are rising rapidly. When the tool is fed to position I, the tool completely enters the machining area. At this time, the cutting temperatures of T_3 and T_1 equal to 102.8 °C and 110.2 °C, respectively. When the tool continues to feed, because the cutting thickness remains unchanged, the temperature begins to enter a stable state. With the accumulation of temperature, the temperature peak value appears in this stage.

Comparing with T_1, T_3 is not only the PCD blades involved in cutting, but also the fish-scale micro-teeth involved in cutting. Therefore, the cutting temperature of T_3 is slightly higher than that of T_1. The temperature peak value of T_3 is 139 °C, which is about 5 °C higher than that of T_1. When the tool is fed to the position II, the slot has been processed and the tool begins to exit. The cutting temperature begins to drop until the tool is completely out of the machining area. The heat conductivity coefficient of the PCD material is 700 W/(m·K) and the heat conductivity coefficient of cemented carbide is 79.6 W/(m·K). Obviously, the conductivity coefficient of the PCD material is nine times higher

(a) Time-varying characteristics of milling temperature
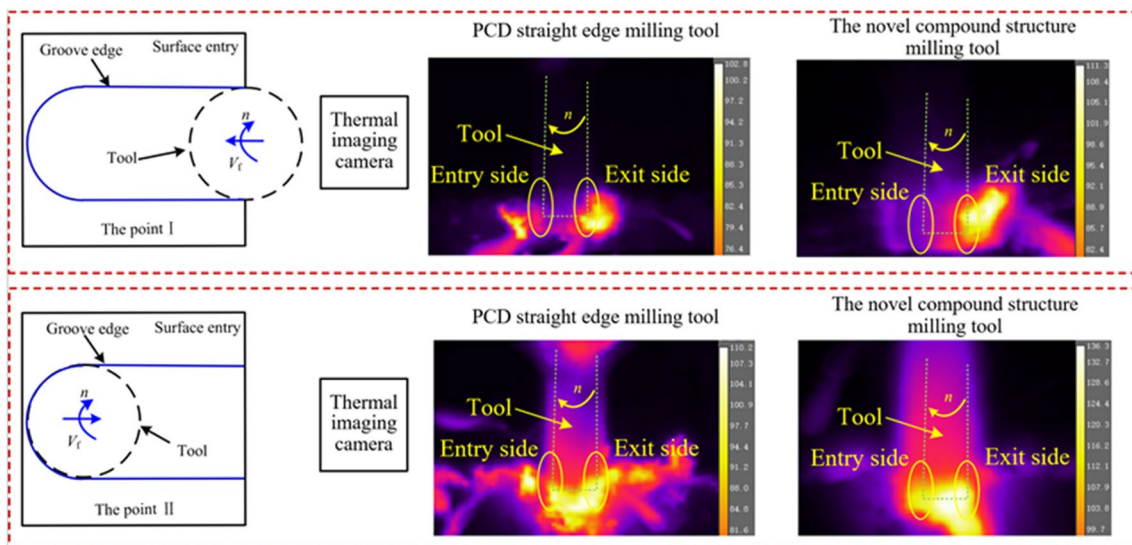
(b) Milling temperatures at different times

Fig. 19 Time-varying characteristics of the cutting side temperature of milling tool of different structures

than that of the cemented carbide. Additionally, the cutting heat by using T_1 focuses at the PCD blades, but the cutting heat by using T_3 focuses at the PCD blades and the fish-scale cutters. Then, the cutting temperature descent of T_3 is a little slower than that of T_1.

5.4.1 Effect of machining parameters on cutting temperature (Fig. 20)

5.5 Comparative analysis of processing quality

5.5.1 The influence of tool structure on machining quality

Under the same processing parameters, the surface quality of KFRP processed by different structures milling tools is shown in Fig. 21. The workpiece surface processed by T_3 has a small number of Kevlar fiber furry defects on the slot edge. Compared to the other two traditional tools, the machining surface quality by using T_3 is best. In T_3, the fish-scale micro-teeth can effectively "pull" the Kevlar fiber in the milling process. And a strong tension can be exerted on the residual fibers by this "pull" effect. Subsequently, the residual fibers can be "sheared" by the PCD blades. The combined action of "pull" and "shear" realizes the goal of reducing furry during the processing of KFRP. According to the above analysis, the cutting temperature of T_3 is higher than that of T_1. The increase in temperature in the process of processing causes the resin matrix to soften and the fiber to lose. When the loose fiber is entangled by the fish-scale micro-tooth, the PCD blades can cut it off in time. Therefore, T_3 can effectively inhibit the production of defects.

Because T_2 lacks the sharp PCD blades, it is difficult to cut off the Kevlar fibers. Therefore, T_2 has the worst surface quality. Based on the experimental observation, the cutting temperature and the feed force are the highest. The resin matrix can be easily destroyed by the high temperature and large feeding
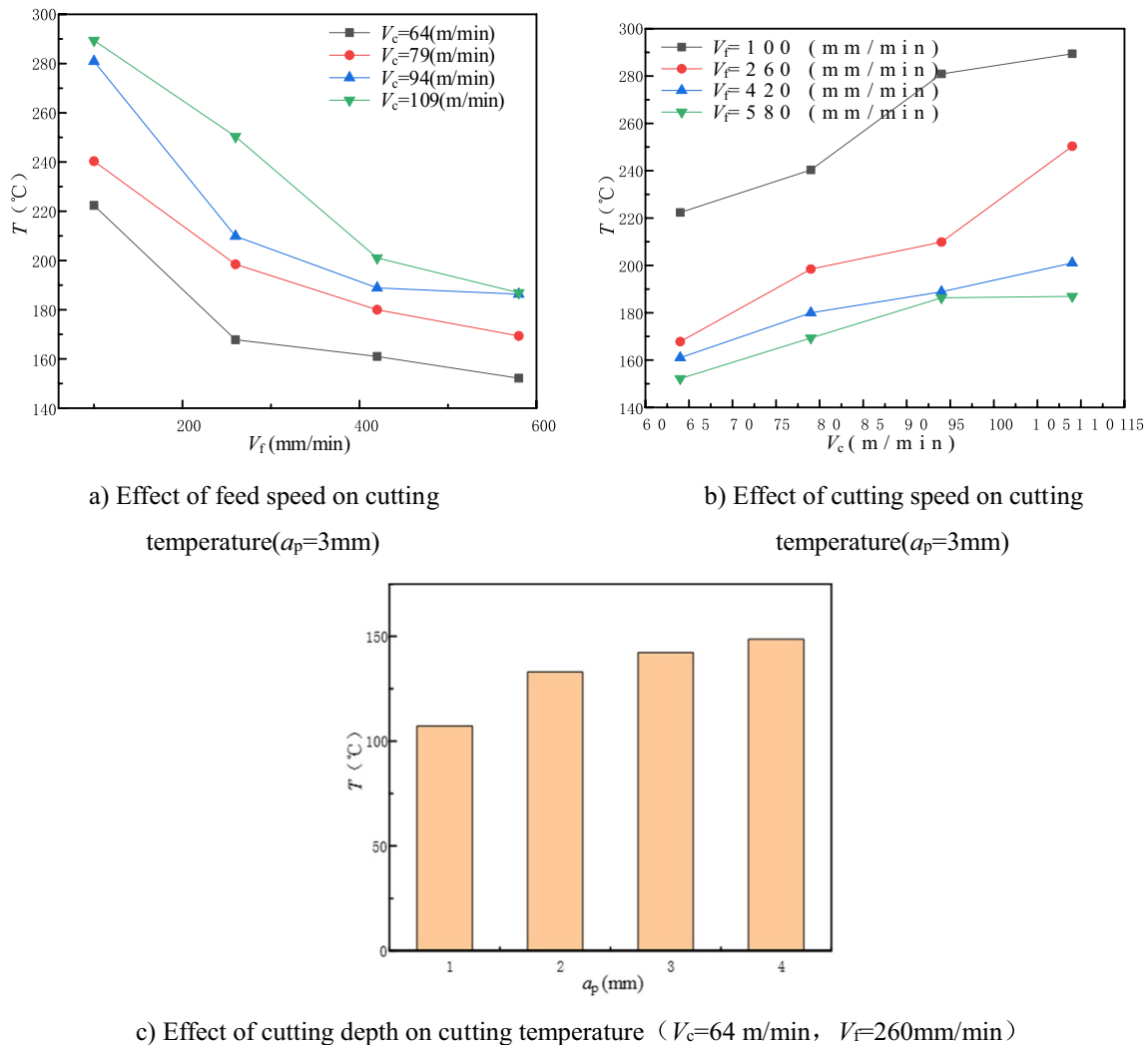

a) Effect of feed speed on cutting
temperature(a_p=3mm)

b) Effect of cutting speed on cutting
temperature(a_p=3mm)

c) Effect of cutting depth on cutting temperature（V_c=64 m/min，V_f=260mm/min）

Fig. 20 Effect of cutting parameters on cutting temperature

force. As a result, a large number of Kevlar fibers loose and furry defects appear.

T_1 mainly benefit from its two sharp blades. The fiber composite materials can be effectively cut off. However, owing to the high cutting temperature and large feed force, the resin matrix is easy to be destroyed. Then, the Kevlar fiber loses the support of the resin. T_1 cannot cut off the residual fibers in time. So T_1 cutting effect is very limited. As a result, the fiber draws furry serious in the cut sides of the groove.

Summarizing the above, the milling surface quality of T_3 is the best. T_1 can effectively cut off the KFRP fibers. But the surface quality of the workpiece surface processed by PCD tool is inferior to T_3. Because the micro-tooth structure causes the Kevlar fibers to lose seriously, T_2 cannot cut off the fibers efficiently. Therefore, the overall cutting surface quality of T_2 is the worst.

After understanding the effect of tool structure on the surface cutting quality, the effect of tool structure on the micromorphological characteristics of KFRP material is further analyzed. Due to the machined surface of T_2 is covered by the residual fibers, the microtopography cannot be easily observed. Thus, the microtopography of the machined surface by using T_2 is not analyzed in this study.

The microscopic morphology of the groove wall machined by T_3 and T_1 under the same process parameters is presented in Fig. 22.

In Fig. 22a, the overall surface is much flatter, with a small amount of fiber furry and rebound phenomenon. However, because the tool overhang is too long and the stiffness of the tool body decreases, the cutting vibration is very serious. In the future, T_3 structure needs to be subsequently improved.

The groove wall processed by T_1 is shown in Fig. 22b. A large number of defects on the surface can be observed. A large number of residual fibers lose the matrix support. Then, these residual fibers cannot be removed. The Kevlar fibers fracture mode is ductile fracture.

5.5.2 Influence of milling parameters on cutting surface quality

As investigated in Fig. 23, the surface quality of milled KFRP is greatly affected by the feed speed. The burr defect factor gradually decreases with the increase of the feed speed. When the cutting speed is 64 m/min, 79 m/min, 94 m/min, and 109 m/min and the feed speed is increased from 100 to 580 mm/min, the burr defect factor
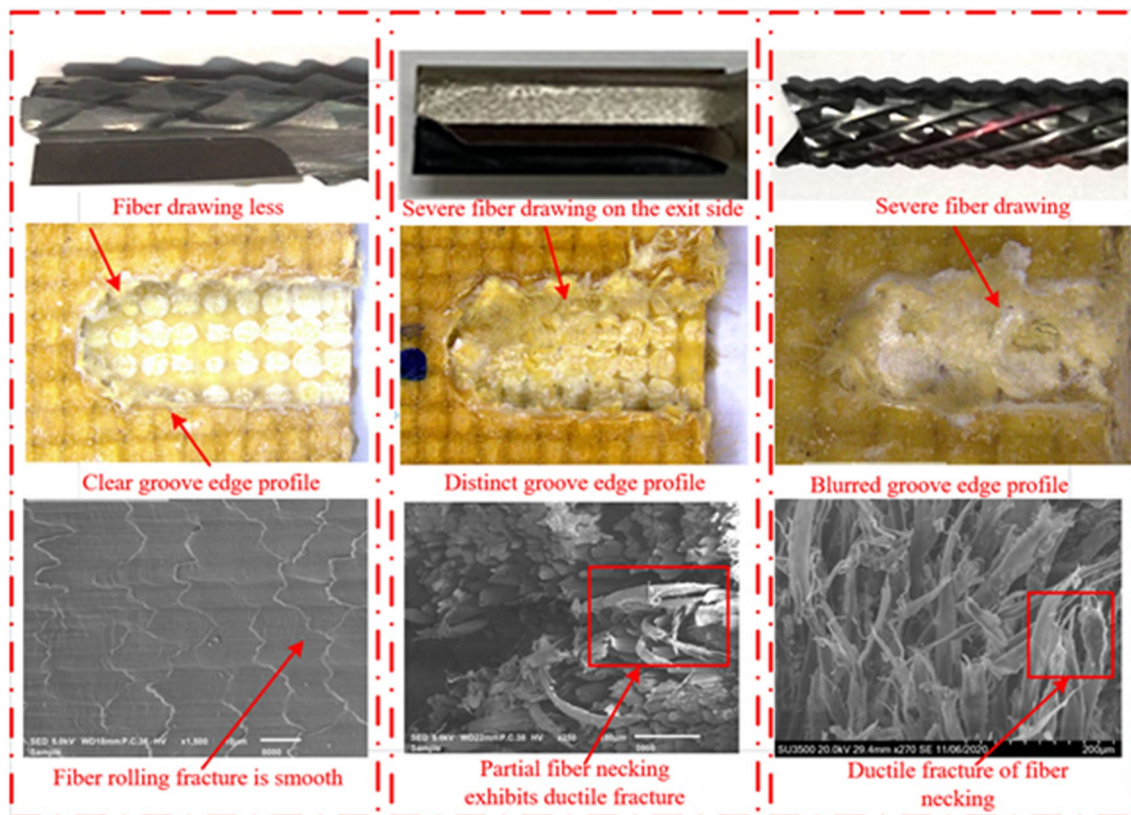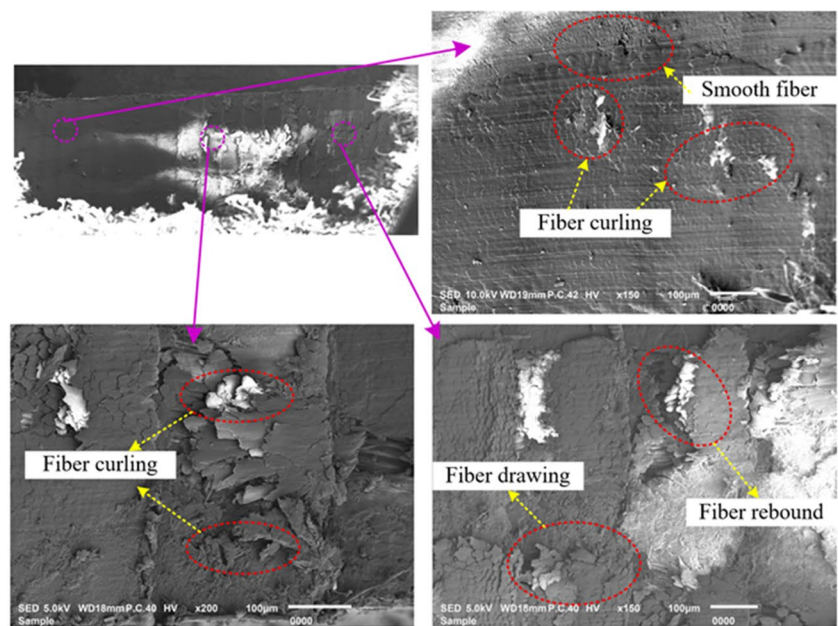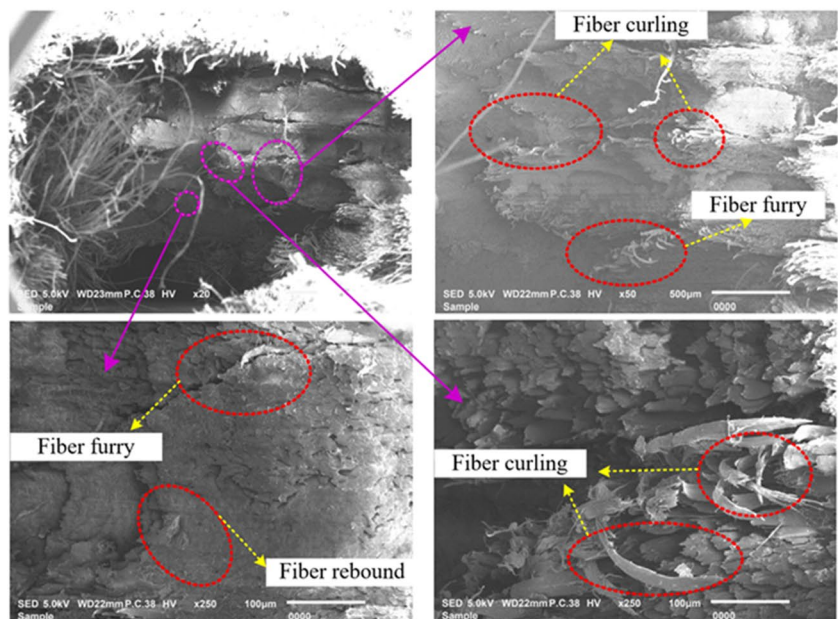

Fig. 21 Effects of different tool structures on machined surfaces (V_c = 64 m/min, V_f = 100 mm/min, a_p = 3 mm)

Fig. 22 Effect of different feeding speed on microscopic cutting surfaces (V_c = 64 m/min, V_f = 100 mm/min, a_p = 3 mm)


(a) Microstructure of T_3

(b) Microstructure of T_1

decreased by 0.44, 0.48, 0.33, and 0.38, respectively. With the increase of the feed speed, the burrs decrease. Additionally, the burrs mainly occur at the fiber junction. According to the previous section, with the increase of the feed speed, the cutting forces increase, but the cutting temperature decreases. The Kevlar fibers can be supported by the undamaged resin, owing to the reduction of the cutting temperature.

As can be seen in Fig. 24, the burr defect factors tend to increase with the increase of cutting speed. When the feed speed is 100 mm/min, 260 mm/min, 420 mm/min, and 580 mm/min and the cutting speed is increased from 64 to 109 mm/min, the burr defect factors decrease by 0.26, 0.43, 0.32, and 0.32, respectively. Low cutting speed, the surface quality is better, the Kevlar fiber furry phenomenon is less. With the increase of cutting speed, the cutting temperature increases

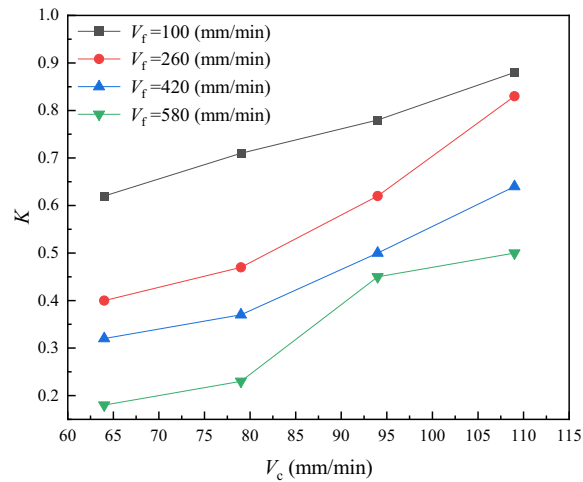**Fig. 23** Effects of different feeding speed on cutting surfaces
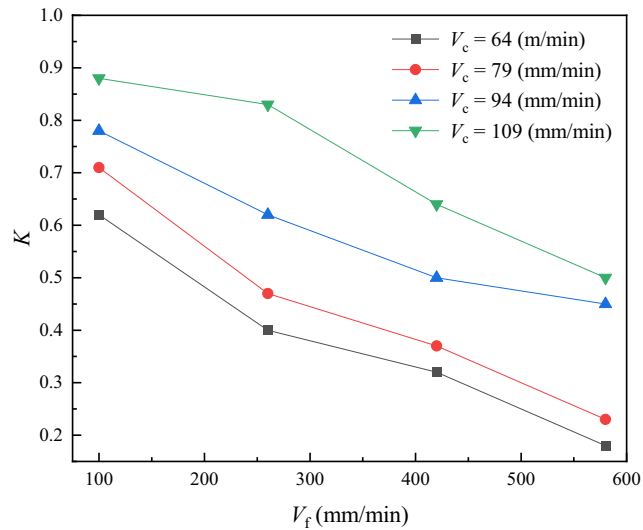
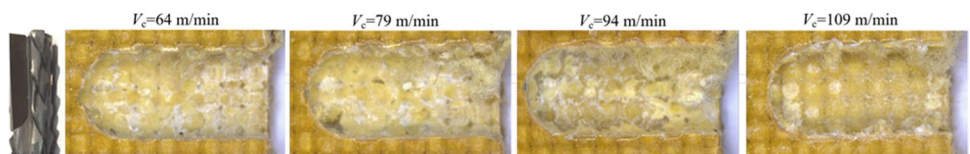(a) The influence of feed speed on the defect factor (a_p=3 mm)
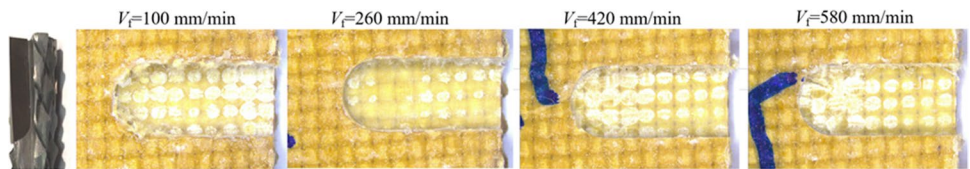
(b) Surface quality of milling (V_c =64 m/min, a_p=3 mm)

Fig. 24 Effects of different cutting speeds on cutting surfaces

(a) The influence of cutting speed on the defect factor (a_p=3 mm)

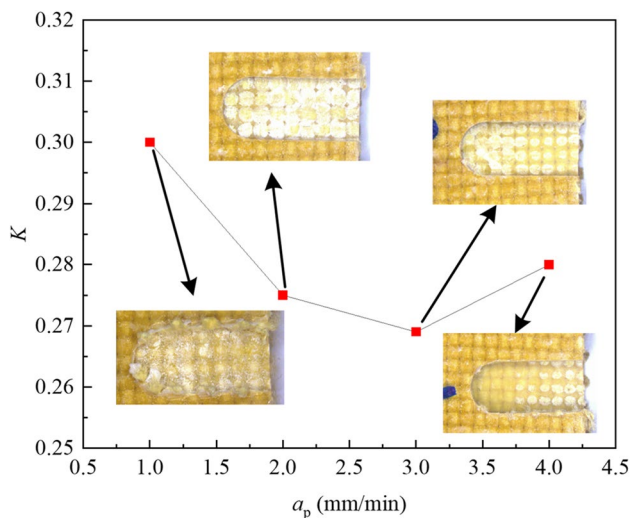(b) Surface quality of milling (V_f =580mm/min, a_p=3 mm)

Fig. 25 Effect of different cutting depth on defect factor (V_c = 64 m/min, V_f = 260 mm/min)

1) When the fibers are subjected to tension, the cutting surface quality is significantly improved. Therefore, when the "pull-shear" removal principle can be implemented effectively, the fibers can be effectively cut off in time.
2) The effect of the novel compound structure tool on the retention of chips and furry is stronger than that of the conventional milling tool. The "pulling-shearing" effect can be effectively implemented by the novel compound structure milling tool. Nevertheless, the cutting parameters need to be selected suitable. The milling surface quality of the novel compound structure milling tool is the best.
3) The cutting forces of the novel compound structure milling tool in a half cycle are superimposed by the other tool cutting forces. The burr defect factor gradually decreases with the increase of the feed speed. And the burrs mainly occur at the fiber junction. The burr defect factors tend to increase with the increase of cutting speed.

gradually. The softening of the resin matrix causes the fiber to lose support, and the furry is difficult to be removed.

The surface milling quality of KFRP is greatly affected by the cutting depth, as observed in Fig. 25. When the cutting depth is 1 mm, the main cutting edge is the PCD blades. There are more Kevlar residual chips and furry can be observed on the machining surface. At this time, the fish-scale micro-tooth structure of T_3 does not play the cutting role. With the increase of cutting depth, the surface quality becomes better, viz., the defect factor decreases. When the cutting depth is 2 mm, part of the fish-scale micro-tooth is involved into the cutting process. The furry on the cut entry side decreases and the furry on the cut exit side increases. When the cutting depth is 3 mm, the fish-scale micro-tooth structure is further added to the cutting process. At this time, the "pull-cut" effect is enhanced and the quality of the machined surface is better. As the cutting depth continues to increase, the milling force and temperature continue to increase. Then, the surface quality began to deteriorate. The Kevlar fibers occur loose and furry. Therefore, the cutting depth needs to be suitable choice.

6 Conclusions

During KFRP cutting, the cutting surface quality is difficult to control. In this paper, the principle of "pull-shear" removing material for furry of fibers was proposed. And a novel compound structure milling tool was designed. Then, the main conclusions are as follows:

Declarations

Ethics approval Authors have read the "Ethical Responsibilities of Authors" and "Compliance with Ethical Standards." This study is an original paper which has neither previously nor simultaneously in whole or in part been submitted anywhere else. Results are presented clearly, honestly, and without fabrication, falsification, or inappropriate data manipulation. Complied fully with the COPE guidelines.

Consent to participate Not applicable.

Consent for publication Not applicable.

Competing interests The authors declare no competing interests.

References

1. Singh TJ, Samanta S (2015) Characterization of Kevlar fiber and its composites: a review. Mater Today: Proc 2(4-5):1381–1387
2. Priyanka P, Dixit A, Mali H (2019) High strength Kevlar fiber reinforced advanced textile composites. Iran Polym J 28(7):621–638

3. Nurazzi NM, Asyraf MRM, Khalina A, Abdullah N, Aisyah HA, Ayu Rafiqah S, Sabaruddin FA, Kamarudin SH, Norrrahim MNF, Ilyas RA, Sapuan SM (2021) A review on natural fiber reinforced polymer composite for bullet proof and ballistic applications. Polymers 13(4):646

4. Bunsell AR (1975) Tensile and fatigue behaviour of Kevlar-49 (PRD-49) fibre. J Mater Sci 10(8):1300–1308

5. Kim SC, Kim JS, Yoon HJ (2011) Experimental and numerical investigations of mode I delamination behaviors of woven fabric composites with carbon, Kevlar and their hybrid fibers. Int J Precis Eng Manuf 12(2):321–329

6. Shi ZY, Cui P, Li X (2019) A review on research progress of machining technologies of carbon fiber-reinforced polymer and aramid fiber-reinforced polymer. Proc Inst Mechanical Eng P C: J Mech Eng Sci 233(13):4508–4520

7. Liu SQ, Chen Y, Fu YC, Hu AD (2016) Study on the cutting force and machined surface quality of milling AFRP. Mater Sci Forum 836:155–160

8. Talib ARA, Ramadhan AA, Rafie ASM, Zahari R (2013) Influence of cut-out hole on multi-layer Kevlar-29/epoxy composite laminated plates. Mater Des 43:89–98

9. Shuaib AN, Al-Sulaiman FA, Hamid F (2004) Machinability of Kevlar® 49 composite laminates while using standard TiN coated HSS drills. Mach Sci Technol 8(3):449–467

10. Teti R (2002) Machining of composite materials. CIRP Ann 51(2):611–634

11. Yilbas BS, Akhtar SS, Karatas C (2017) Laser circular cutting of Kevlar sheets: analysis of thermal stress filed and assessment of cutting geometry. Opt Laser Technol 96:180–189

12. Shi ZY, Duan NM, Li X, Wang ZH (2020) Analysis and control of surface delamination defects during milling of orthogonal aramid fiber-reinforced composites laminates. Trans Nanjing Univ Aeronaut Astronaut 37(03):353–359

13. Wang FB, Liu JK, Shu QL (2017) Optimization of cryogenic milling parameters for AFRP. Int J Adv Manuf Technol 91:9–12

14. Wang DH, Ramulu M, Arola D (1995) Orthogonal cutting mechanisms of graphite/epoxy composite part 1: unidirectional laminate. Int J Mach Tools Manuf 35(12):1623–1638

15. Dandekar CR, Shin YC (2008) Multiphase finite element modeling of machining unidirectional composites: prediction of debonding and fiber damage. J Manuf Sci Eng 130(5):611–622

16. Calzada KA, Kapoor SG, DeVor RE, Samuel J, Srivastava AK (2012) Modeling and interpretation of fiber orientation-based failure mechanisms in machining of carbon fiber-reinforced polymer composites. J Manuf Process 14(2):141–149

17. Xu J, Feng P, Feng F, Zha H, Liang G (2021) Subsurface damage and burr improvements of aramid fiber reinforced plastics by using longitudinal–torsional ultrasonic vibration milling. J Mater Process Technol 297:117265

18. Cheng H, Gao J, Kafka OL, Zhang K, Luo B, Liu WK (2017) A micro-scale cutting model for UD CFRP composites with thermo-mechanical coupling. Compos Sci Technol 153:18–31

19. Chen R, Li SJ, Li PN, Liu X, Qiu XP, Tae JK, Jiang Y (2020) Effect of fiber orientation angles on the material removal behavior of CFRP during cutting process by multi-scale characterization. Int J Adv Manuf Technol 106(11):5017–5031

20. Xu J, Deng Y, Wang CX, Liang GQ (2021) Numerical model of unidirectional CFRP in machining: development of an amended friction model. Compos Struct 256(113075):1–11

21. Alessandro A, Sein LS, Khamis E (2017) Modelling the orthogonal cutting of UD-CFRP composites: development of a novel cohesive zone model. Compos sturct 168:65–83

22. Meng QX, Cai J, Cheng H, Zhang KF (2020) Investigation of CFRP cutting mechanism variation and the induced effects on cutting response and damage distribution. Int J Adv Manuf Technol 106:2893–2907

23. Bhattacharyya D, Horrigan DPW (1998) A study of hole drilling in Kevlar composites. Compos Sci Technol 58(2):267–283

24. Yan T, Shi W, Li J, Wang L, Xie C, Dong L, Ma T (2023) Experimental study and simulation analysis of the fracture mechanism in AFRP milling. Proc I MechE Part C: J Mechanical Eng Sci 1–15

25. Qi B (2019) Research on drilling force model of KFRP. IOP Conference Series: Mater Sci Eng 563(3):032046

26. Swan S, Jacob J, Dave K, Dinh N, Patrick K (2018) Tool wear of advanced coated tools in drilling of CFRP. J Manuf Sci Eng 140(11):111018

27. Jia ZY, Fu R, Niu B, Qian BW, Bai Y, Wang FJ (2016) Novel drill structure for damage reduction in drilling CFRP composites. Int J Mach Tools Manuf 110:55–65

28. Qiu XY, Li PN, Li CP, Niu QL, Chen AH, Ouyang PR, Ko TJ (2019) New compound drill bit for damage reduction in drilling CFRP. Int J Precision Eng Manuf-Green Technol 6(1):75–87

29. Gao S (2021) Design and experimental research of ultra- precision fly-cutting processing suction chip exhaust system. Harbin University of Science and Technology